Quasi-normal free-surface impacts and capillary walking

C. A. Galeano-Rios, P. A. Milewski and J.-M. Vanden-Broeck

[1]Department of Mathematical Sciences, University of Bath, Bath, BA2 7AY, UK

[1]Department of Mathematics, University College London, London WCIE 6BT, UK

Quasi-normal free-surface impacts, capillary rebounds and application to Faraday walkers.

C. A. Galeano-Rios[1] C.A.Galeano.Rios@bath.ac.uk, P. A. Milewski[1]
J.-M. Vanden-Broeck[2]

June 12, 2019

Abstract

We present a model for capillary-scale objects that bounce on a fluid bath as they also translate horizontally. The rebounding objects are hydrophobic spheres that impact the interface of a bath of incompressible fluid whose motion is described by linearised quasi-potential flow. Under a quasi-normal impact assumption, we demonstrate that the problem can be decomposed into an axisymmetric impact onto a quiescent bath surface, and the unforced evolution of the surface waves. We obtain a walking model that is free of impact parametrisation and we apply this formulation to model droplets walking on a vibrating bath. We show that this model accurately reproduces experimental reports of bouncing modes, impact phases, and time-dependent wave field topography for bouncing and walking droplets. Moreover, we revisit the modelling of horizontal drag during droplet impacts to incorporate the effects of the changes in the pressed area during droplet-surface contacts. Finally, we show that this model captures the recently discovered phenomenon of *superwalkers*.

capillary waves, drops, wave-structure interactions.

1 Introduction

Examples of millimetric objects bouncing on the surface of a bath as they cruise along the surface are common in capillary scale applications; these include raindrop impacts (Zhbankova & Kolpakov, 1990; Ho *et al.*, 1997) and locomotion of insects and small vertebrates (Bush & Hu, 2006). In the case of droplets, it was shown by Couder *et al.* (2005*a*) that coalescence with an underlying bath of the same fluid can be inhibited through vertical oscillation of the bath. The droplet is prevented from merging with the bath by the sustenance of a thin air layer that separates the two at all times (Couder *et al.*, 2005*a*; Terwagne *et al.*, 2007). These droplets can bounce for extremely long times, displaying different bouncing regimes which are controlled by the amplitude and frequency of the shaking. Moreover, within a certain range of parameters, these bouncing droplets can become unstable to horizontal perturbations (Couder *et al.*, 2005*b*),

breaking the axial symmetry of the surface wave field. Droplets then bounce off a slanted free surface, acquiring a horizontal velocity component and thus start *walking* along a straight path.

Walking droplets are affected at each bounce by the wave field at the impact location. Since these waves were triggered by previous bounces, the droplet is in practice interacting with a record of its own trajectory. This droplet-wave association at millimetric scale has come to be known as a *hydrodynamic pilot-wave* (Bush, 2015). Hydrodynamic pilot-waves exhibit complex dynamics that have been shown to have numerous analogies with quantum-scale phenomena (Bush *et al.*, 2018), which motivated their study by several groups over the past 14 years. Some examples of models created to address walking droplet dynamics include a first phenomenological model by Eddi *et al.* (2011), a nonlinear spring based surface-droplet interaction by Moláček & Bush (2013*b*), a *stroboscopic* model introduced by Oza *et al.* (2013) and a model that introduced wave generation by impacts by Milewski *et al.* (2015).

Galeano-Rios *et al.* (2017) developed a model for the impact of a hydrophobic sphere onto the free surface of a bath. Their impact model modified the Wagner theory of surface impacts (Wagner, 1932; Korobkin & Pukhnachov, 1988; Howison *et al.*, 1991) to account for the reaction of the impacting solid to forces exerted by the flow, including capillary effects, and to intrinsically allow for a mechanism for the impacting solid to detach from the surface. This resulted in a model that can solve all stages of a rebounding impact at the capillary scale, provided the surface deformation is not too large. They essentially imposed a *kinematic match* between the motion of the free surface and that of the impacting sphere, i.e. they imposed the natural geometric and kinematic constraints, together with simple assumptions on the contact angle, to derive a solution strategy that yields predictions for the motion of the contact line and for the pressure field supported within the contact area. Their impact model was validated against experimental results and they went on to show that it can be used to accurately predict the vertical motion of bouncing droplets whilst also introducing fewer assumptions on the nature of the impact and, consequently, fewer parameters than in previous works (Moláček & Bush, 2013*a*; Milewski *et al.*, 2015).

Superposing translations of axisymmetric impacts on linear quasi-potential free surface flows has proven to be a highly effective strategy to model walking droplets (Moláček & Bush, 2013*b*; Oza *et al.*, 2013; Milewski *et al.*, 2015). This approximation is justified on the basis of some clear separation of scales; namely, the Faraday wave length ($\lambda_F \approx 0.5\,\mathrm{cm}$) is long in relation to the droplet radius ($R_o \approx 0.4\,\mathrm{mm}$), the droplet radius is in turn large in relation to the typical free-surface elevation ($\epsilon \lesssim 10\,\mu\mathrm{m}$ at impact location just before contact), moreover the walking speed ($C_w \approx 1\,\mathrm{cm/s}$) is slow in relation to the phase velocity of the Faraday waves ($C_p \approx 20\,\mathrm{cm/s}$) and also to the typical vertical velocity of the impacting droplet ($U_z \approx 10\,\mathrm{cm/s}$). Under these assumptions, vertical forces can be calculated assuming the impact is normal to a flat horizontal surface. The horizontal component of the impact forces on the droplet can then be computed assuming these impact forces are actually normal to the relatively small local

average of the surface gradient in the region of impact.

The *kinematic match* method is very versatile, and is applicable to impact problems with no assumptions on symmetry; however, its implementation in such a general case is more complex. In this paper; we demonstrate that, under the assumptions above, we may approximate the dynamics by a superposition of translated axisymmetric impacts. Using the kinematic match for these axisymmetric impacts results in a more detailed and realistic modelling of the walking droplets, in relation to existing methods, whilst also providing information about the fastest time-scales in the problem, such as those of the evolution of forces and of the pressed area during impacts.

In this work, we also demonstrate how to combine an efficient solution of the large-scale non-axisymmetric free-surface waves using a spectral method developed in Milewski *et al.* (2015) with the superposition of axisymmetric impacts described above, so as to obtain an accurate and efficient model for walking droplets that is free of any impact parametrisation. The decomposition here introduced opens many new possibilities, as there are no restricting assumptions on the geometry of the bath, or the presence of neighbouring droplets. This is fundamental to simulate collective behaviour of bouncing and walking droplets as keeping the details of wave generation by impact has proven to be fundamental to capture wave mediated droplet-droplet interactions (Galeano-Rios *et al.*, 2018).

In section 2, we pose the full problem, presenting the kinematic match method, expanding the discussion in Galeano-Rios *et al.* (2017), and reviewing the linearised quasi-potential fluid model. We close this section justifying the superposition of translations of axisymmetric impacts to obtain a model for walking droplets and deriving a model for friction effects during droplet-surface contacts that is consistent with the theory developed here and that incorporates changes in pressed area over droplet-surface contacts. In section 3 we summarise the resulting mathematical problems, describe the numerical methods used to solve each, and the recombination of their results. We also show how we use experimental data to set our single parameter for skidding friction during droplet contacts. In section 4 we present comparisons to experimental data available in the literature, including bouncing modes, impact and take off phases and wave field topography, and we show that our model is able to capture the newly discovered walking-droplet phenomenon of *superwalkers* (Valani *et al.*, 2019). In the case of superwalkers we are specifically able to capture the transition from bouncing to walking as the second frequency is introduced, and to obtain wave fields that qualitatively resemble that of superwalkers. We highlight that we were unable to obtain realistic results with the model introduced by Milewski *et al.* (2015). Finally, in section 5 we discuss our findings and consider future directions.

2 Problem formulation

We consider the three-dimensional, free-surface, incompressible flow of a fluid bath of infinite depth and uniform density ρ. The fluid flow is subject to gravitational, viscous and interfacial forces. We introduce Cartesian coordinates with gravity pointing in the negative z direction. We also assume that the free surface can be described by $z = \eta(\boldsymbol{x}, t)$, where $\boldsymbol{x} = (x, y)$, whose spatial domain is the entire plane. We define $\boldsymbol{u}$ and p as the velocity and pressure fields, respectively, ν as the kinematic viscosity of the fluid and $\boldsymbol{g} = (0, 0, -G)$ as the acceleration due to gravity. We note that G can be a function of time. Under these assumptions, the flow is governed by

$$\boldsymbol{u}_t + \boldsymbol{u} \cdot \boldsymbol{\nabla} \boldsymbol{u} = \boldsymbol{\nabla} \left(-\frac{p}{\rho} \right) + \nu \Delta \boldsymbol{u} + \boldsymbol{g}, \quad z \leq \eta(\boldsymbol{x}, t); \tag{1}$$

$$\boldsymbol{\nabla} \cdot \boldsymbol{u} = 0, \quad z \leq \eta(\boldsymbol{x}, t). \tag{2}$$

The velocity field $\boldsymbol{u}$ is subject to decay conditions at infinity

$$\boldsymbol{u} \to 0, \text{ as } \sqrt{x^2 + y^2 + z^2} \to \infty, \tag{3}$$

and the free surface is subject to the kinematic boundary condition

$$\eta_t + \boldsymbol{u} \cdot \boldsymbol{\nabla}(\eta - z) = 0, \quad z = \eta(\boldsymbol{x}, t); \tag{4}$$

and the dynamic boundary condition

$$-p\hat{\boldsymbol{n}} + T \cdot \hat{\boldsymbol{n}} = (\sigma \, \kappa[\eta] - p_s(\boldsymbol{x}, t)) \, \hat{\boldsymbol{n}}, \quad z = \eta(\boldsymbol{x}, t); \tag{5}$$

where $\hat{\boldsymbol{n}}$ is the unitary vector normal to the free surface, pointing out of the fluid domain; T is the deviatoric part of the stress tensor; p_s is the pressure above the free surface; σ is the surface tension coefficient; and $\kappa[\cdot]$ is twice the mean curvature operator, with the convention of positive curvature for convex functions, i.e.

$$\kappa[\eta] = \frac{\left(1 + \eta_y^2\right) \eta_{xx} - 2\eta_x \eta_y \eta_{xy} + \left(1 + \eta_x^2\right) \eta_{yy}}{\left(1 + \eta_x^2 + \eta_y^2\right)^{3/2}}. \tag{6}$$

We define $h(t)$ as the height of the lowest point, the "south pole", of the impacting sphere, c_f as the coefficient of friction due to air drag on the sphere, m_s as the mass of the impacting object, and we consider $p_s(\boldsymbol{x}, t) = 0$ everywhere outside the area that is pressed by the impacting solid. In the pressed area $A(t)$, we disregard the thickness of the air layer separating the surface of the bath and the sphere; i.e. $A(t) \in \mathbb{R}^2$ is the projection onto the xy-plane of the set $S(t)$, which is given by the part of the surface of the impacting object that coincides with the free surface of the bath. Consequently, we have

$$h_{tt} = -G - \frac{c_f}{m_s} h_t + \frac{1}{m_s} \int_{A(t)} p_s \mathrm{d}A. \tag{7}$$

5

We denote by $z_s(\boldsymbol{x})$ the height of the lower half of the sphere, such that $z_s(\boldsymbol{X}) = 0$, with $\boldsymbol{X} = (X, Y)$ being the horizontal coordinates of the south pole of the sphere. On the contact line $L(t)$, i.e. the boundary of $A(t)$, we define ∂_n as the derivative in the direction normal to $L(t)$ which points outside of the plane region $A(t)$. We impose continuity of the free-surface gradient on $L(t)$, as would be expected in the presence of an intervening air layer. Solutions must therefore satisfy

$$p_s(\boldsymbol{x}, t) = 0, \quad \boldsymbol{x} \notin A(t); \tag{8}$$

$$\eta(\boldsymbol{x}, t) = h(t) + z_s(\boldsymbol{x}), \quad \boldsymbol{x} \in A(t); \tag{9}$$

$$\eta(\boldsymbol{x}, t) < h(t) + z_s(\boldsymbol{x}), \quad \boldsymbol{x} \notin A(t); \tag{10}$$

$$\partial_n \eta(\boldsymbol{x}, t) = \partial_n z_s(\boldsymbol{x}), \quad \boldsymbol{x} \in L(t); \tag{11}$$

where we define $z_s(\boldsymbol{x}) = \infty$ away from the sphere. We emphasise that equations (8), (9), (10) and (11) simply state the minimal compatibility conditions consistent with a model that ignores the effects of the air flow in the lubrication layer. We also note that equation (11) corresponds to our assumption of perfect hydrophobicity. This assumption is based on the established fact that there is an intervening air layer separating droplet and bath (Couder *et al.*, 2005*a*), and therefore no contact angle smaller than π is to be expected. It is worth mentioning that it is possible to modify this condition to allow for different, or even dynamic, contact angles.

We highlight that determining $A(t)$, is itself a part of the problem; that is to say that finding the pressure field and its domain is a two-dimensional free-boundary problem within our original three-dimensional free-boundary fluid-flow problem. Moreover, the problem of the pressure field is a free-boundary problem with an added difficulty, given that the domain of the pressure actually collapses to a point upon lift-off and re-appears from a point when a new impact takes place.

2.1 Solving the two free-boundary problems

The algorithm presented in Galeano-Rios *et al.* (2017) solves the problem of the suddenly appearing pressed area and its subsequent evolution upon the impact of a solid. Moreover, the method is able to deal with the vanishing contact area when lift-off takes place. We review it in what follows. We first consider, for simplicity, the solid to be fixed as the free surface impacts on it. That is to say, we consider the case of $h(t)$ being constant and solving the system given by (1)-(11), disregarding (7) initially. We then discuss how (7) is introduced.

We consider the free surface of a fluid bath which, at a time $t = t_0$, approaches a fixed, perfectly hydrophobic solid, shown in figure 1(a). In order to calculate the free-surface elevation at a certain time $t_0 + \delta t$, we need to solve the free boundary problem over the time interval $t \in [t_0, t_0 + \delta t]$. First, we tentatively impose $p_s(\boldsymbol{x}, t) = 0$ and we solve the system given by (1)-(6); if the solution satisfies (10) everywhere (i.e. predicts no contact or overlap between
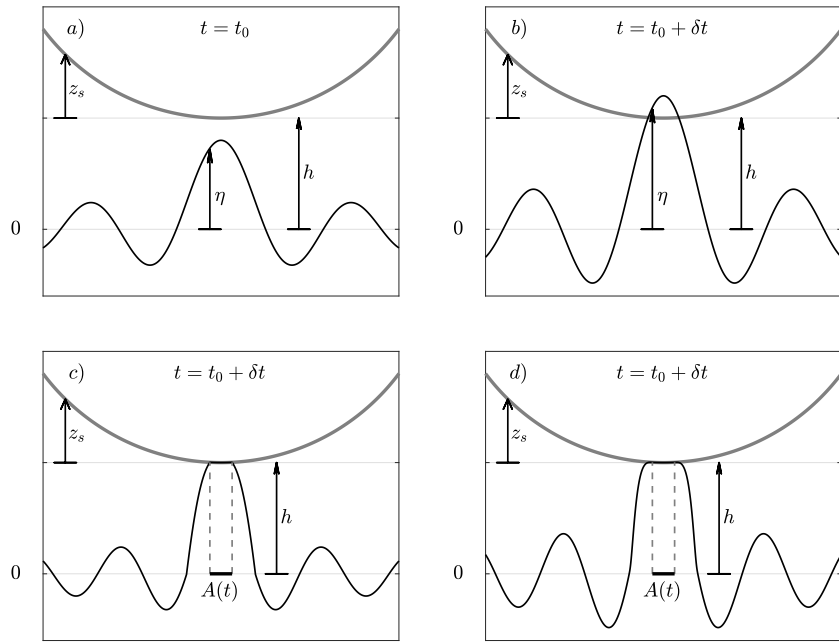
Figure 1: Schematics of onset of contact as solved by the *kinematic match* method. The boundary of the fixed solid, given by z_s, is shown in grey; and the fluid interface, given by η, in black. The height of the solid surface z_s is measured with respect to that of its lowest point h. Panels show: regular evolution with no pressed area (a), inconsistent estimate of free surface at $t = t_0 + \delta t$ (b), tentative solution for $t = t_0 + \delta t$ with an A_{test} that yields a wrong contact angle (c), and solution with an A_{test} that yields the right contact angle (d).

the fluid and the solid), then it trivially solves the remaining conditions of system (1)-(11). However, if (as in the example of figure 1) our prediction for the location of the free surface at time $t_0 + \delta t$ suggests that part of the fluid occupies the same space as the solid, then we have not obtained a solution to (1)-(11) and an impact must have occurred, see figure 1(b). The evolution of the free surface should have been constrained by the presence of the solid and there should be a region within which $p_s(\boldsymbol{x}, t)$ was not identically zero over the interval $[t_0, t_0 + \delta t]$.

In order to find a correct solution to system (1)-(11), and since $A(t_0 + \delta t)$ is to be determined, we proceed by testing a contact area candidate A_{test}. We assume the contact area changes continuously, therefore A_{test} must be small at the onset of contact. We solve the system for η everywhere outside A_{test}, and for the value of p_s on A_{test} (where η is known). The method exchanges the known and unknown variables in the pressed area, yielding a closed problem for system (1)-(9) at $t_0 + \delta t$. Naturally, the solution to (1)-(9), obtained assuming $A(t + \delta t) = A_{\text{test}}$ might not satisfy (10) or (11), since this was just an initial choice, so we need to verify these. If either condition is not satisfied we repeat the process using a new A_{test}, obtained by perturbing our prior choice until the solution satisfies (10) and (11) (see figures 1(c) and 1(d)).

At a time $t = t_1$, when the fluid is in contact with the solid (i.e. $A(t_1) \neq \emptyset$), we proceed with the method in a similar manner. For time $t_1 + \delta t$ we iterate on our candidate pressed areas A_{test}, chosen in the vicinity of $A(t_1)$, and we solve system (1)-(9) for each A_{test} until we verify (10) and (11). We note that, if $A(t_1)$ is relatively small, the empty set is considered to be in its vicinity and therefore we include the possibility of $A_{\text{test}} = \emptyset$, i.e. $p_s(\boldsymbol{x}, t) = 0$.

When the impacting object is able to move vertically, the problem involves the response of the fluid forces onto it and we still need to iterate on the contact area; however, we no longer know *a priori* the exact elevation of the free surface η on A_{test}. Nevertheless, we know η up to a vertical translation, given by $h(t)$. This vertical translation adds an unknown to the system, but we also add (7), which closes the problem (1)-(9) for a given A_{test} at $t = t_0 + \delta t$. We can thus iterate on A_{test} once again, and stop the iteration when (10) and (11) are satisfied.

2.2 The linearised model

2.2.1 Linearised fluid equations

Following Galeano-Rios *et al.* (2017) we use a linearised quasi-potential approximation of the fluid flow, with $\boldsymbol{u}$ defined on the domain $D = \{(\boldsymbol{x}, z), z \leq 0\}$, where $z = 0$ is the undisturbed free-surface level. We define; $\varphi(\boldsymbol{x}, z, t)$ as the velocity potential; Δ_H as the two-dimensional Laplacian, i.e. $\Delta_H = \partial_{xx} + \partial_{yy}$; and N as the Dirichlet-to-Neumann operator, given by

$$N\varphi(\boldsymbol{x}, 0, t) = \varphi_z(\boldsymbol{x}, 0, t). \tag{12}$$

In formulating the Faraday wave problem, g as the gravity constant, a as

8

the amplitude of the vertical shaking and ω_o as its angular frequency. The fluid viscosity ν is corrected to ν^* in order to use a quasi-potential approximation whilst still matching the driving amplitude at which the Faraday threshold is observed. For the parameter regime at which we run simulations (see Appendix A), $\nu^* = 0.8025\nu$ (Milewski et $al.$, 2015). Adopting the Faraday wavelength λ_F as the unit length, the reciprocal of the subharmonic Faraday wave frequency f_F^{-1} as the unit time, and $\rho\lambda_F^3$ as the unit mass, where ρ is the density of the bath's fluid. We also define

$$Fr = \lambda_F f_F^2/g, \ We = \rho\lambda_F^3 f_F^2/\sigma, \ \Gamma = a\omega_o^2/g, \ Re = \lambda_F^2 f_F/\nu^*; \qquad (13)$$

and $\phi(\boldsymbol{x}, t) = \varphi(\boldsymbol{x}, 0, t)$.

The free surface can be shown to evolve (Galeano-Rios et $al.$, 2017) according to

$$\eta_t = \frac{2}{Re}\Delta_H\eta + N\phi, \qquad (14)$$

$$\phi_t = -\frac{(1 - \Gamma\cos(4\pi t))}{Fr}\eta + \frac{1}{We}\kappa[\eta] + \frac{2}{Re}\Delta_H\phi - p_s, \qquad (15)$$

subject to

$$\eta \to 0, \ \text{when} \ \sqrt{x^2 + y^2} \to \infty; \qquad (16)$$

$$\phi \to 0, \ \text{when} \ \sqrt{x^2 + z^2} \to \infty. \qquad (17)$$

We note that these equations describe the free surface in the frame of reference of the moving bath, which introduces a time dependent coefficient in (15), and that the curvature κ is not yet linearised. In fact, we will retain the full curvature in the contact area, where it is $O(1)$ and known a $priori$ from the geometry of the solid, as was done in Galeano-Rios et $al.$ (2017).

2.2.2 Vertical dynamics of the sphere

We recall that m_s is the mass of the droplet and define μ_{air} as the dynamic viscosity of air; R_o as the droplet radius and h^c as the height of the centre of mass, which yields $h = (h^c - R_o)/\lambda_F$ as the dimensionless height of the south pole of the sphere. We approximate the effects of air on the moving droplet using Stokes' drag and we introduce the dimensionless quantities

$$Ma = m_s/\left(\rho\lambda_F^3\right), \qquad So = 6\pi\mu_{\text{air}}R_o/(m_s f_F). \qquad (18)$$

We thus have

$$h_{tt} = -\frac{(1 - \Gamma\cos(4\pi t))}{Fr} - So\, h_t + \frac{1}{Ma}\int_{A(t)} p_s \mathrm{d}A. \qquad (19)$$

We describe the lower half of the impacting sphere, in dimensionless variables, using

$$z_s(\boldsymbol{x}) = \begin{cases} \frac{R_o}{\lambda_F} - \sqrt{\frac{R_o^2}{\lambda_F^2} - |\boldsymbol{x}|^2} & |\boldsymbol{x}| \leq \frac{R_o}{\lambda_F}, \\ \\ \infty & |\boldsymbol{x}| > \frac{R_o}{\lambda_F}; \end{cases} \qquad (20)$$

thus, given the horizontal location of the centre of mass as $\boldsymbol{X}(t) = (X(t), Y(t))$, we can re-write constraints (8)-(11) as

$$p_s = 0, \quad \boldsymbol{x} \notin A(t); \tag{21}$$

$$\eta(\boldsymbol{x}, t) = h(t) + z_s\left(\boldsymbol{x} - \boldsymbol{X}(t)\right), \quad \boldsymbol{x} \in A(t); \tag{22}$$

$$\eta(\boldsymbol{x}, t) < h(t) + z_s\left(\boldsymbol{x} - \boldsymbol{X}(t)\right), \quad \boldsymbol{x} \notin A(t); \tag{23}$$

$$\partial_n \eta(\boldsymbol{x}, t) = \partial_n z_s\left(\boldsymbol{x} - \boldsymbol{X}(t)\right), \quad \boldsymbol{x} \in L(t). \tag{24}$$

The horizontal trajectory $\boldsymbol{X}(t)$ is naturally dependent on the surface waves, and it needs to be coupled to system (14)-(24) to close the problem. For the sake of clarity, we present the horizontal dynamics in detail, later in the text.

We highlight that, whilst the problem given by (14)-(24) is linear during each droplet flight, the problem remains highly non-linear during impacts. The implicit non-linearity takes place through the free-boundary problem for the pressure and the pressed area.

2.3 Approximation by superposition of normal impacts

We now introduce a further approximation to the problem, namely we consider impacts to be quasi-normal to the surface. This approximation was used by all previous works on walking droplets; however, the arguments that follow constitute (to the best of our knowledge) the first mathematical justification for it.

As mentioned in section 1, the walking velocity of droplets ($C_w \approx 1\,\text{cm/s}$) is typically small relative to the vertical velocity of impact ($U_z \approx 10\,\text{cm/s}$). This means that impacts are nearly vertical and that the difference between imposing condition (22) exactly and approximately (i.e. using the simplification that $\boldsymbol{X}(t)$ is constant during the impact) is of the order of the distance that the droplet moved during contact with the bath times the gradient of z_s (bottom half of a sphere). Moreover, the linear approximation to surface deflection allows for the problem to be decomposed into a vertical (i.e. almost normal) impact on an initially quiescent interface and the unforced evolution of the waves.

We consider the time $t = t_0$ at which impact is imminent and we re-write equation (22), in dimensionless units, as for $t \in (t_0, t_l)$:

$$\eta(\boldsymbol{x}, t) = h(t) + z_s\left(\boldsymbol{x} - \boldsymbol{X}(t_0)\right) + \left[z_s\left(\boldsymbol{x} - \boldsymbol{X}(t)\right) - z_s\left(\boldsymbol{x} - \boldsymbol{X}(t_0)\right)\right], \quad \boldsymbol{x} \in A(t); \tag{25}$$

where we know the term in brackets to be of $O(|\nabla z_s|C_w(t_l - t_0)/\lambda_F)$, where t_l is the time at which lift off happens with $t_l - t_0 < T_F/2$ (typically), and C_w is the typical speed of a walking droplet, which is small with respect to the phase velocity of the waves $C_p = \lambda_F/T_F$. Moreover, for the case of an impacting sphere, when the pressed radius is less than half the radius of the sphere (as is the typical case for walking droplets) $|\nabla z_s|$ is at most $O(1)$. Therefore the term in brackets is at most $O(C_w/C_p)$ (typically $C_w/C_p \approx 0.05$) and thus, we can conclude that, near the impact location, we can impose an axisymmetric

kinematic condition (by ignoring the term in brackets) with an error of at most this order.

We now rewrite the quasi-normal impact as the superposition of three different problems. Problem a, given by the axisymmetric impact of a sphere onto the quiescent surface of a bath; problem b defined by the unforced wave field evolution of the free surface without the ongoing impact, and problem r, given by the remaining terms in the full problem. More specifically, we define problems a and b, such that

$$\eta = \eta^a + \eta^b + \eta^r, \tag{26}$$

$$\phi = \phi^a + \phi^b + \phi^r, \tag{27}$$

$$h(t) = h^a(t) + \eta^b(\boldsymbol{X}(t), t) + h^r(t); \tag{28}$$

where the super-indexes a and b indicate the solution of each problem and r is the remainder with respect to the solution of the full impact problem (14)-(24). First, for $t \in [t_0, t_l]$, we define the homogeneous problem b as

$$\eta_t^b = \frac{2}{Re}\Delta_H \eta^b + N\phi^b, \tag{29}$$

$$\phi_t^b = -\frac{(1 - \Gamma\cos(4\pi t))}{Fr}\eta^b + \frac{1}{We}\Delta_H\eta^b + \frac{2}{Re}\Delta_H\phi^b, \tag{30}$$

subject to $\eta^b \to 0$, when $\boldsymbol{x} \to \infty$; and $\phi^b \to 0$, when $\boldsymbol{x} \to \infty$; with

$$\eta^b(\boldsymbol{x}, t_0) = \eta(\boldsymbol{x}, t_0), \quad \text{and} \quad \phi^b(\boldsymbol{x}, t_0) = \phi(\boldsymbol{x}, t_0). \tag{31}$$

That is to say, problem b gives the evolution of the fluid flow as if the impact that occurs in the time interval $[t_0, t_l]$ does not take place. We highlight that, due to the finite wave speed, outside the vicinity of the impact location, problem b is in fact the full problem.

We can then re-write equation (25) using equation (26) and subtract $\eta^b(\boldsymbol{X}(t), t)$ from both sides to obtain

$$\eta^a(\boldsymbol{x}, t) + \left[\eta^b(\boldsymbol{x}, t) - \eta^b(\boldsymbol{X}(t), t)\right] + \eta^r(\boldsymbol{x}, t) =$$
$$\left[h(t) - \eta^b(\boldsymbol{X}(t), t)\right] + z_s(\boldsymbol{x} - \boldsymbol{X}(t_0)) + O(C_w/C_p); \tag{32}$$

where the term in brackets on the right hand side of equation (32) will be used to define h^a as used in equation (28). Namely, for $t \in [t_0, t_l]$, we define the axisymmetric impact problem a as

$$\eta_t^a = \frac{2}{Re}\Delta_H\eta^a + N\phi^a, \tag{33}$$

$$\phi_t^a = -\frac{(1 - \Gamma\cos(\omega_o t))}{Fr}\eta^a + \frac{1}{We}\kappa[\eta^a] + \frac{2}{Re}\Delta_H\phi^a - p_s^a, \tag{34}$$

$$h_{tt}^a = -\frac{(1 - \Gamma\cos(4\pi t))}{Fr} - So\,h_t^a + \frac{1}{Ma}\int_{A^a(t)} p_s^a \mathrm{d}A^a; \tag{35}$$

subject to $\eta^a \to 0$, when $|\boldsymbol{x}| \to \infty$; $\phi^a \to 0$, when $\boldsymbol{x} \to \infty$; and

$$\eta^a(\boldsymbol{x}, t) = h^a(t) + z_s(\boldsymbol{x} - \boldsymbol{X}(t_0)), \quad \boldsymbol{x} \in A^a(t); \quad (36)$$

$$\eta^a(\boldsymbol{x}, t) < h^a(t) + z_s(\boldsymbol{x} - \boldsymbol{X}(t_0)), \quad \boldsymbol{x} \notin A^a(t); \quad (37)$$

$$p_s^a(\boldsymbol{x}, t) = 0, \quad \boldsymbol{x} \notin A^a(t); \quad (38)$$

$$\partial_n \eta^a(\boldsymbol{x}, t) = \partial_n z_s(\boldsymbol{x} - \boldsymbol{X}(t_0)), \quad \boldsymbol{x} \in L^a(t); \quad (39)$$

with

$$\eta^a(\boldsymbol{x}, t_0) = 0, \quad \text{and} \quad \phi^a(\boldsymbol{x}, t_0) = 0 \quad (40)$$

and

$$h^a(t_0) = h(t_0) - \eta^b\left(\boldsymbol{X}(t_0), t_0\right), \qquad h_t^a(t_0) = h_t(t_0) - \eta_t^b\left(\boldsymbol{X}(t_0), t_0\right). \quad (41)$$

Hence, problem a is given by an axisymmetric impact on an undisturbed quiescent free surface, which preserves the relative initial height and relative incoming velocity from the full impact problem. Moreover, we assume that the contact area is simply connected, which (under the axial symmetry assumption) translates into the axisymmetric approximation $A^a(t)$ (of the full-problem contact area $A(t)$) being a disc.

We also know that the term in brackets on the left hand side of equation (32) is such that

$$\left[\eta^b(\boldsymbol{x}, t) - \eta^b\left(\boldsymbol{X}(t), t\right)\right] = O(\epsilon R_o/\lambda_F^2), \quad (42)$$

where ϵ is the typical amplitude of the wave and equation (42) is in dimensionless units. We note that typically $\epsilon R_o/(\lambda_F^2) \approx 1.5 \times 10^{-4}$. This shows that the remainder, η^r, must be at most of $O(\epsilon R_o/\lambda_F^2) + O(C_w/C_p)$. We note that η^r is given by problem r

$$\eta_t^r = \frac{2}{Re}\Delta_H \eta^r + N\phi^r, \quad (43)$$

$$\phi_t^r = -\frac{(1 - \Gamma\cos(4\pi t))}{Fr}\eta^r + \frac{1}{We}\Delta_H \eta^r + \frac{2}{Re}\Delta_H \phi^r - (p_s - p_s^a)$$
$$+ (\kappa - \Delta_H)\left[\eta^a + \eta^b + \eta^r\right] - (\kappa - \Delta_H)\left[\eta^a\right], \quad (44)$$

with

$$\eta^r(\boldsymbol{x}, t_0) = 0, \quad \text{and} \quad \phi^r(\boldsymbol{x}, t_0) = 0. \quad (45)$$

It is important to mention that problem r, can only be solved *a posteriori*, as it needs function p_s which is obtained from the full problem (14)-(24). Nevertheless, equations (43) and (44) show that when the pressure is well approximated by that of an axisymmetric impact and when the curvature of the unforced problem is small, the remainder problem r is the result of weakly forced problem for which we expect to observe very small waves. In what follows, we approximate the problem by the sum of problem a and problem b, that is to say, we disregard the residual term in equations (26)-(28). We note that the resulting approximation yields a continuous solution for η, ϕ and h.
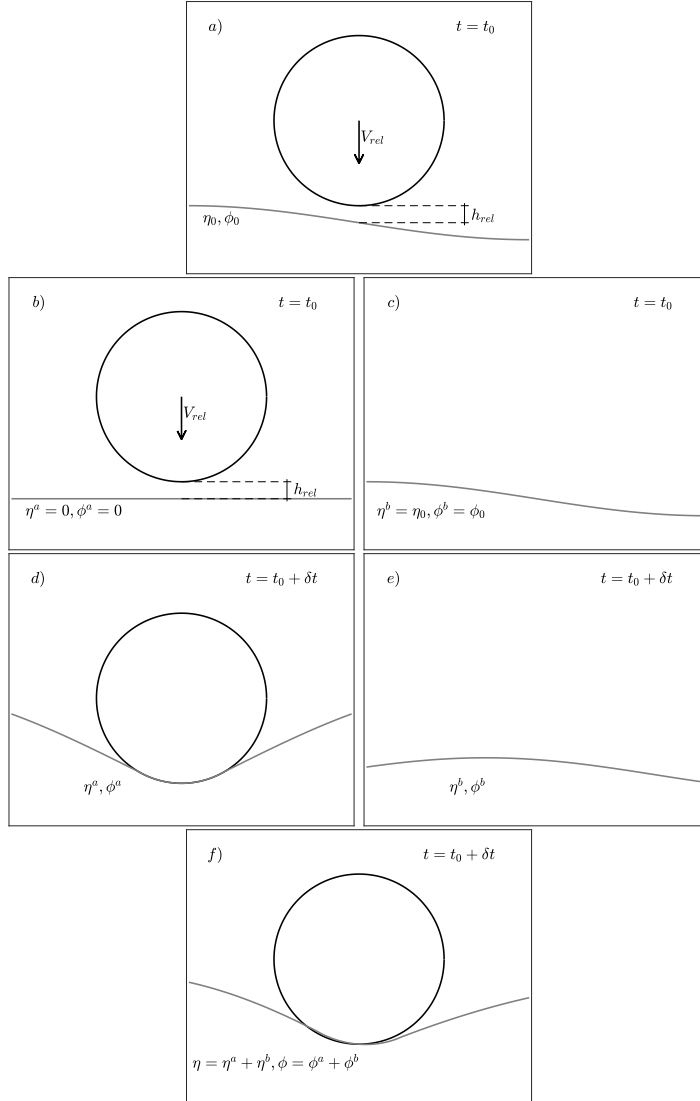
Figure 2: Schematics of the decomposition of the impact of a walking droplet problem into two simpler calculations. Panel (a) shows the initial conditions given by an imminent droplet impact, (b) and (c) show the initial conditions for each of the separate problems, (d) and (e) respectively show the evolution of (b) and (c), and (f) shows how the results (d) and (e) are combined. The sub-index rel indicates magnitudes measured in relation to the point of the free surface that is directly below the south pole of the sphere.

13

In summary, we model the wave field of a walking droplet by superposing translations of axisymmetric wave fields due to droplet impacts. When the droplet is in flight we calculate the free surface evolution by solving the linear equations (14) and (15), with $\kappa = \Delta_H$, and the droplet height from equation (19); all subject to $p_s(\boldsymbol{x}, t) = 0$. When an impact is about to happen, we separate the problem into two (see figure 2). We define problem a as the axisymmetric impact of a droplet onto a bath, with the initial conditions of $\eta^a(\boldsymbol{x}, t_0) = 0$, $\phi^a(\boldsymbol{x}, t_0) = 0$, and the position and velocity of the droplet being such that the relative height and vertical velocity with respect to the surface point exactly below the south pole are the same as in the physical problem (figures 2(b) and 2(d)). For this problem, we preserve the full curvature κ within $A(t)$, as done in Galeano-Rios $et\ al.$ (2017). We solve the axisymmetric problem a until the droplet is once again airborne. In parallel, we define problem b in which we find waves η^b, ϕ^b with initial conditions $\eta^b(\boldsymbol{x}, t_0) = \eta(\boldsymbol{x}, t_0)$, $\phi^b(\boldsymbol{x}, t_0) = \phi(\boldsymbol{x}, t_0)$, but without the pressure induced by the droplet, which is to say we ignore the forcing of the ongoing droplet contact as we solve the wave field (figures 2(c) and 2(e)). The temporally dependent nature of gravity is preserved in both problems. We then superpose the axisymmetric solution of the droplet impact on the unforced surface waves at the predicted location of the droplet $\boldsymbol{X}(t)$. Once the droplet is again in flight we carry on solving a single problem, namely that resulting from the superposition.

We note that the vertical droplet motion obtained from the impact on the flat free surface is treated as an approximation to the motion of the actual droplet relative to the point on the fluid surface that is directly under the south pole of the droplet. That is to say, that the height and velocities of the droplet as obtained from the impact of a flat interface will be added to the height and velocity of the fluid surface at the $\boldsymbol{X}(t)$ location in order to obtain the prediction for the height of the droplet for $t \in [t_0, t_l]$. We highlight that this superposition does not result in a perfect match of the surfaces (see figure 2(f)); however, it still yields an exact match between the south pole of the droplet and the corresponding point of the free surface. The mismatch between the sphere and the free surface of the bath is of the order of the wave gradient in problem b, i.e. $\epsilon/\lambda_F = O(10^{-3})$, times the radius of the typical pressed area ($\leq 0.5 R_o$). Therefore, the typical mismatch of $O(10^{-3})$ when expressed as a fraction of the droplet radius.

2.4 Horizontal dynamics

We derive equations for the horizontal motion of the sphere on the basis of the approximations introduced in section 2.3. For impacts, we arrive at a model that includes the horizontal components of the pressure forces that were previously discussed in section 2.2.2, as well as a drag force due to a simplified model of viscous forces in the intervening air layer similar to the one presented in Couder $et\ al.$ (2005a) and Protière $et\ al.$ (2006). The main advantage of the derivation presented in what follows is that we are able to include the effect of changes in pressed area over each contact of the droplet.

The horizontal motion of the droplet, expressed in dimensionless variables, is governed by

$$\mathbf{X}_{tt} = \frac{1}{Ma} \left(\int\limits_{A(t)} \frac{-p_s \nabla\eta}{\sqrt{1+|\nabla\eta|^2}} \mathrm{d}A + \int\limits_{S(t)} (T_{\mathrm{air}} \cdot \hat{\boldsymbol{n}})_H \mathrm{d}S + \int\limits_{S^2 \setminus S(t)} (-p_{\mathrm{air}}\hat{\boldsymbol{n}} + T_{\mathrm{air}} \cdot \hat{\boldsymbol{n}})_H \mathrm{d}S \right),$$
(46)

where T_{air} is the deviatoric part of the stress tensor for the air flow, $\hat{\boldsymbol{n}}$ is the outward pointing unit normal to the sphere, p_{air} is the air pressure, the sub-index H indicates the projection onto the xy-plane, S^2 is the surface of the whole sphere, and we recall that $A(t)$ is the horizontal projection of $S(t)$, the portion of the sphere's surface that is in contact with the free surface of the bath. The first term in the parenthesis on the right hand side of equation (46) corresponds to horizontal forces due to pressure between the two free surfaces; the second corresponds to the horizontal component of the viscous effects of the flow of air in the intervening layer; the third term accounts for the contribution of horizontal forces due to the air, outside of the pressed area.

Given the scaling considerations discussed in section 2.3, the leading order term for the pressure forces due to impact yields

$$-\frac{1}{Ma} \int_{A(t)} p_s \frac{\nabla\eta}{\sqrt{1+|\nabla\eta|^2}} \mathrm{d}A \approx -\nabla\eta^b|_{(\boldsymbol{X}(t),t)} \frac{1}{Ma} \int_{A^a(t)} p_s^a \mathrm{d}A, \qquad (47)$$

where we have also used the assumption that, since surface waves are long when compared to the droplet diameter, the local average of the gradient is approximately equal to $\nabla\eta^b(\boldsymbol{X}(t),t)$.

Since we are not simulating the air flow, we approximate the effect of the deviatoric stresses within the pressed area by

$$\frac{1}{Ma} \int\limits_{A(t)} (T_{\mathrm{air}} \cdot \hat{\boldsymbol{n}})_H \sqrt{1+|\nabla\eta|^2} \mathrm{d}A \approx -\frac{E(t) T_F}{m_s} \boldsymbol{X}_t, \qquad (48)$$

with $E(t)$ being a skidding friction coefficient whose form we discuss below. The third term is approximated using Stokes' drag, assuming the pressed area is a relatively small fraction of the surface area of the sphere, hence

$$\frac{1}{Ma} \int\limits_{S^2 \setminus S(t)} (-p_{\mathrm{air}}\hat{\boldsymbol{n}} + T_{\mathrm{air}} \cdot \hat{\boldsymbol{n}})_H dS \approx So\, \boldsymbol{X}_t, \qquad (49)$$

with So as in equation (18). We thus have

$$\boldsymbol{X}_{tt} = -D(t)\boldsymbol{X}_t - \nabla\eta^b|_{(\boldsymbol{X}(t),t)} \frac{1}{Ma} \int_{A^a(t)} p_s^a \mathrm{d}A, \qquad (50)$$

where $D(t) = So + E(t)/(f_F m)$. We note that, during impacts, the term So (due to Stokes' drag) is negligible.

15

2.4.1 Skidding friction

Realistic modelling of skidding friction due to the air flow within the lubrication layer requires methods that can solve a free-boundary lubrication theory problem on a curved, non-symmetric geometry that deforms, and whose deformation is coupled to droplet and wave motion. Moreover, it is the non-symmetric part of the solution to this problem that must be responsible for drag in walking droplets. Given the complexity of this problem, prior works have introduced different simplifications to address this effect; for instance Moláček & Bush (2013b) introduced a scaling argument based on the assumption of a constant pressed area and experimental observations of the horizontal coefficient of restitution in single droplet impacts on a flat interface.

We recall that our model yields a time-dependent pressed area approximation as part of the solution to the axisymmetric problem a. This allows for the construction of the first skidding friction model that accounts for the effects of the changes in the pressed area during impacts. We thus revisit skidding friction modelling and we are able to derive a working approximation which yields slightly improved predictions (in terms of comparison to experiments) on the existing methods and also offers an explanation as to why two competing approaches used in the past by other groups can be seen as expressions of the same effect when we account for changes in the pressed area over an impact.

Assuming the pressed area $A(t)$ is small enough that the part of the sphere in contact with the free-surface is almost flat, viscous friction forces in the thin air layer would be approximately given, in dimensional variables, by

$$F_D = -\mu_{\text{air}}|A(t)|\,\overline{\partial_z \mathbf{u}_H|_{(z=\eta)}}, \tag{51}$$

where μ_{air} is the dynamic viscosity of air, $|A(t)|$ is the surface area of $A(t)$, $\mathbf{u}_H$ is the horizontal velocity of the air, and the bar indicates the mean in the contact area. The expression under the bar should scale as $\mathbf{X}_t/e$, where e is the width of the air layer, which we assume does not change substantially during the contact time. We thus make the following approximation

$$F_D = -\bar{k}\mu_{\text{air}}|A(t)|\frac{\mathbf{X}_t}{e} \approx -k\mu_{\text{air}}|A^a(t)|\frac{\mathbf{X}_t}{R_o}, \tag{52}$$

where $\bar{k}$ is a scaling factor for the vertical derivative of the horizontal velocity which we absorb into $k = \bar{k}R_o/e$, a drag parameter. Moreover, we approximate the pressed area $A(t)$ by its the circlular $A^a(t)$. We note that for a typical droplet radius ($R_o \approx 0.4$ mm) and for the typical air layer width ($e \approx 2$ μm) as predicted in Protière et al. (2006), we obtain $R_o/e \approx 200$, which suggest that the values of the dimensionless coefficient k should be of order $O(100\bar{k})$.

In principle, k could be different for each value of driving acceleration or even impact velocity and impact phase, as well as other factors; however, in the present work, we will treat k as constant with respect to those variables. Consequently, in equation (48), we estimate

$$E(t) = k\frac{\mu_{\text{air}}}{R_o}|A^a(t)|, \tag{53}$$

which in equation (50), in dimensionless variables, yields

$$\boldsymbol{X}_{tt} = -\frac{3Da}{4Ra}\left(6 + k\frac{|A^a(t)|}{\pi R_o^2}\right)\boldsymbol{X}_t - \nabla\eta^b|_{(\boldsymbol{x},t)}\frac{1}{Ma}\int_{A^a(t)} p_s^a \mathrm{d}A, \qquad (54)$$

where $Ra = R_o^2 f_F/\nu_{\mathrm{air}}$ and $Da = \rho_{\mathrm{air}}/\rho$, with ν_{air} and ρ_{air} being the kinematic viscosity and the density of air, respectively. We note that the only undetermined parameter in this equation is k, whose value we set as described later in the text. We anticipate however, that the term $k\frac{|A^a(t)|}{\pi R_o^2}$ will dominate the drag effect, in accordance with the relatively minor effect that air drag during flight has shown to have, for instance using the model of Milewski *et al.* (2015) we see nearly unchanging waking speeds with or without Stokes' drag.

3 Solution

For completeness, and given the complexity of the full model, we summarise it below together with a discussion of the numerical techniques used.

When the droplet is in flight we solve

$$\eta_t = \frac{2}{Re}\Delta_H\eta + N\phi, \qquad (55)$$

$$\phi_t = -\frac{(1 - \Gamma\cos(4\pi t))}{Fr}\eta + \frac{1}{We}\Delta_H\eta + \frac{2}{Re}\Delta_H\phi, \qquad (56)$$

$$h_{tt} = -\frac{(1 - \Gamma\cos(4\pi t))}{Fr} - So\, h_t; \qquad (57)$$

$$\boldsymbol{X}_{tt} = -\frac{9Da}{2Ra}\boldsymbol{X}_t; \qquad (58)$$

for η, ϕ, h and $\boldsymbol{X}$. This is done using a spectral method in space, a second order Runge-Kutta method in time for equations (55) and (56) with a fixed time step, following Milewski *et al.* (2015); and exact integration for equations (57) and (58). Care is taken to ensure that the periodic domain used in the spectral method is large enough to guarantee that the waves have decayed at the boundary, mimicking the conditions $\eta \to 0$, when $\sqrt{x^2 + y^2} \to \infty$; and $\phi \to 0$, when $\sqrt{x^2 + y^2} \to \infty$. More specifically, we find that a domain of $40\lambda_F \times 40\lambda_F$ is sufficient for all simulations considered here, the spatial mesh for the unforced wave field is set to have $2^{11} \times 2^{11}$ points, and the regular temporal mesh is set to have 80 time steps per Faraday period.

When the method described above yields $h(t) \leq \eta(\boldsymbol{X}(t), t)$, i.e. the sphere and the bath are overlapping, we discard this solution and we define the previous time step as $t = t_0$. We then define

$$\eta^a(\boldsymbol{x}, t_0) = 0, \qquad \eta^b(\boldsymbol{x}, t_0) = \eta(\boldsymbol{x}, t_0), \qquad (59)$$

$$\phi^a(\boldsymbol{x}, t_0) = 0, \qquad \phi^b(\boldsymbol{x}, t_0) = \phi(\boldsymbol{x}, t_0), \qquad (60)$$

$$h^a(t_0) = h(t_0) - \eta(\boldsymbol{X}(t_0), t_0), \qquad h^b(t_0) = \eta^b(\boldsymbol{X}(t_0), t_0), \qquad (61)$$

$$h_t^a(t_0) = h_t(t_0) - \eta_t(\boldsymbol{X}(t_0), t_0), \qquad h_t^b(t_0) = \eta_t^b(\boldsymbol{X}(t_0), t_0), \qquad (62)$$

17

and we solve independent problems for initial conditions a and b.

The axisymmetric, forced problem for the impact is given by

$$\eta_t^a = \frac{2}{Re}\Delta_H \eta^a + N\phi^a, \quad z = 0; \tag{63}$$

$$\phi_t^a = -\frac{(1 - \Gamma\cos(4\pi t))}{Fr}\eta^a + \frac{1}{We}\kappa[\eta^a] + \frac{2}{Re}\Delta_H\phi^a - p_s^a, \quad z = 0; \tag{64}$$

$$h_{tt}^a = -\frac{(1 - \Gamma\cos(4\pi t))}{Fr} - So\,h_t^a + \frac{1}{Ma}\int_{A^a(t)} p_s^a\mathrm{d}A; \tag{65}$$

subject to $\eta^a \to 0$, when $\sqrt{x^2 + y^2} \to \infty$; $\phi^a \to 0$, when $\sqrt{x^2 + y^2 + z^2} \to \infty$; and

$$\eta^a(\boldsymbol{x}, t) = h^a(t) + z_s(\boldsymbol{x}), \quad \boldsymbol{x} \in A^a(t); \tag{66}$$

$$\eta^a(\boldsymbol{x}, t) < h^a(t) + z_s(\boldsymbol{x}), \quad \boldsymbol{x} \notin A^a(t); \tag{67}$$

$$p_s^a(\boldsymbol{x}, t) = 0, \quad \boldsymbol{x} \notin A^a(t); \tag{68}$$

$$\partial_n \eta^a(\boldsymbol{x}, t) = \partial_n z_s(\boldsymbol{x}), \quad \boldsymbol{x} \in L^a(t); \tag{69}$$

whilst also assuming that $\kappa[\eta^a(\boldsymbol{x}, t)] \approx \Delta_H \eta^a(\boldsymbol{x}, t)$, when $\boldsymbol{x} \notin A^a(t)$. This problem is solved using finite differences and a numerical approximation to the singular integral operator N (following Galeano-Rios *et al.* (2017)), in space; and implicit Euler in time, with an adaptive time step. The axisymmetric domain size is set to $2\lambda_F$, the spatial mesh size is set for each droplet size to $R_o/40$, and the adaptive time step is always chosen as a refinement of the temporal mesh of the unforced problem. The solution to this problem is calculated until $t = t_l$, by which the droplet is once again in flight.

In parallel, we solve the homogeneous non-axisymmetric problem

$$\eta_t^b = \frac{2}{Re}\Delta_H\eta^b + N\phi^b, \tag{70}$$

$$\phi_t^b = -\frac{(1 - \Gamma\cos(4\pi t))}{Fr}\eta^b + \frac{1}{We}\Delta_H\eta^b + \frac{2}{Re}\Delta_H\phi^b, \tag{71}$$

subject to $\eta^b \to 0$, when $\sqrt{x^2 + y^2} \to \infty$; and $\phi^b \to 0$, when $\sqrt{x^2 + y^2} \to \infty$, from $t = t_0$ to $t = t_l$; and we define

$$h^b(t) = \eta^b(\boldsymbol{X}(t), t), \qquad h_t^b(t) = \eta_t^b(\boldsymbol{X}(t), t), \tag{72}$$

for $t \in [t_0, t_l]$.

The horizontal motion of the particle for $t \in [t_0, t_l]$ is computed by solving

$$\boldsymbol{X}_{tt} = -\frac{3Da}{4Ra}\left(6 + k\frac{|A^a(t)|}{\pi R_o^2}\right)\boldsymbol{X}_t - \nabla\eta^b|_{(\boldsymbol{X}(t), t)}\frac{1}{Ma}\int_{A^a(t)} p_s^a\mathrm{d}A; \tag{73}$$

with a semi-implicit Euler method.

The solutions η, ϕ, h, h_t for $t \in [t_0, t_l]$ are thus given by

$$\eta(\boldsymbol{x}, t) = \eta^a \left(\boldsymbol{x} - \boldsymbol{X}(t), t\right) + \eta^b(\boldsymbol{x}, t), \tag{74}$$

$$\phi(\boldsymbol{x}, t) = \phi^a \left(\boldsymbol{x} - \boldsymbol{X}(t), t\right) + \phi^b(\boldsymbol{x}, t), \tag{75}$$

$$h(t) = h^a(t) + h^b(t), \tag{76}$$

$$h_t(t) = h_t^a(t) + h_t^b(t); \tag{77}$$

at which point the droplet is once again in flight and we can repeat the procedure.

In summary, when an impact is about to take place, we first solve an axisymmetric impact until a time which we define as t_l, when the droplet has lifted off. From this problem, we find the vertical forces on the droplet and the surface deflection due to the impact. In parallel, we evolve the unforced surface waves until $t = t_l$. We take the information of the surface elevation gradient of the unforced waves, at the location given by the droplet position, and we compute the horizontal motion of the droplet. Finally, we superpose the axisymmetric wave from problem a to the solution of problem b, at the corresponding location $\boldsymbol{X}(t)$.

There are several advantages to the approach taken here. For instance, the impact problem can be solved in a smaller domain, as this domain only needs to be large enough to guarantee that the waves have not reached its boundary over the duration of an impact. This allows for a much finer mesh, with respect to that reported in Galeano-Rios *et al.* (2017), to be used to solve the impact problem whilst still allowing much faster computations. Conversely, the wave propagation without the impact can be solved using a much coarser mesh than was used in Galeano-Rios *et al.* (2017), since the typical wavelength is large in comparison to the droplet. More importantly, we are able to use a Fourier method for the unforced waves, which diagonalises the Laplacian operators. Similarly, we can use a much finer time step for the impacts, which allows for an improved resolution of the vertical forces on the droplet with respect to what was obtained in Galeano-Rios *et al.* (2017), whilst we use a coarser time mesh for the unforced wave-propagation problem, allowing for faster computations. In section 4, we show that the approximation method described above also provides increased accuracy.

3.1 Simulations

Simulations are initiated by imparting the droplet with a horizontal velocity of $0.1\ C_p$ and with a downward vertical velocity that is in the typical range for walking droplets; all while the droplet is slightly above the surface. Droplets will then settle onto a steady walking speed or come to a halt, if the system parameters do not allow steady walking. We are able to identify the known bouncing modes which we describe with the ordered pairs (m, n), following Gilet & Bush (2009) and Moláček & Bush (2013a), in which m stands for the number of forcing periods contained in a complete period of vertical motion,
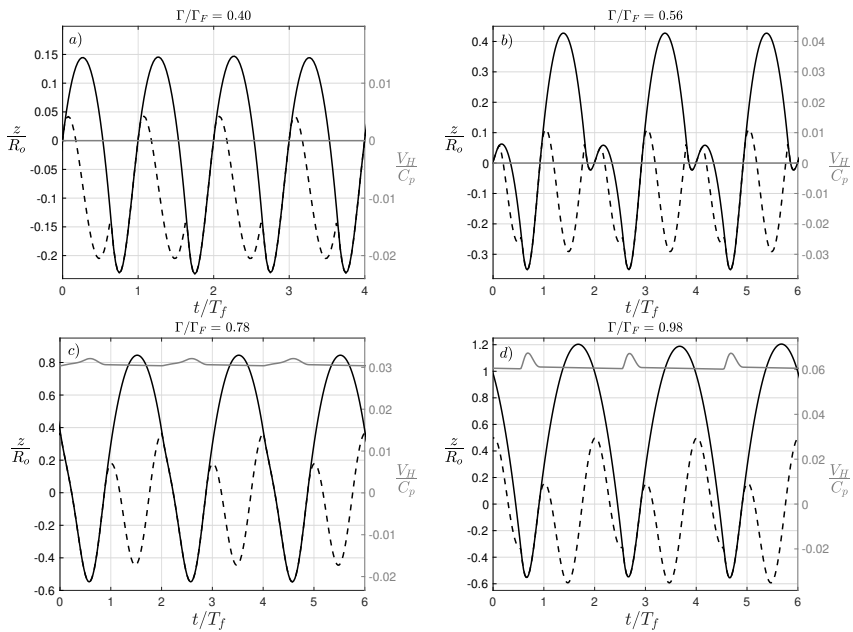
Figure 3: Simulation results for droplets walking at different driving accelerations (Γ). Solid black lines show the trajectory of the south pole of the droplet and dashed lines correspond to the point of the free surface just under the south pole. Grey lines show the horizontal speed of the droplets. C_p is the phase velocity of the Faraday waves ($C_p = 19.88 \, \text{cm/s}$), and T_f is the forcing period. Both panels correspond to a droplet of radius $R_o = 0.38 \, \text{mm}$, i.e. vibration number $\Omega = 0.8$ ($\Omega = \omega_o \sqrt{\rho R_o^3 / \sigma}$) and drag parameter $k = 3100$. Panels (a), (b), (c) and (d) correspond to modes $(1,1)$, $(2,2)$, $(2,1)^1$ and $(2,1)^2$, respectively.

20

and n corresponds to the number of contacts that take place during m forcing periods. These different modes can be identified in figure 3, in which droplet contacts correspond to the time intervals over which the south pole coincides with the free surface. We are also able to distinguish variants within the same (m, n) mode, such as the $(2, 1)^1$ and $(2, 1)^2$ (see figures 3c and 3d). We discuss the distinction of these modes in greater detail later in the text.

Figure 4 shows the simulation of the wave fields of a bouncer and a walker, which display the typical features reported in Eddi *et al.* (2011). We highlight that the vertical scale in panels c-f is largely exaggerated in order to provide a quantitative comparison of the scales of the unforced waves and the impact dimple. This might create the illusion of a non-smooth interface. The inset plot in panels c and d (for which we use the same scale in x and z) show that the free surface is in fact very smooth. Animations of the simulations presented in figure 4 are provided as supplementary material, these also clearly portray the surface smoothness.

We run simulations of walking droplets in the parameter regimes investigated experimentally by previous works (Wind-Willassen *et al.*, 2013; Moláček & Bush, 2013*b*; Pucci *et al.*, 2016) with the experimental set up of 20 cSt and 80 Hz (see Appendix A) for different values of the vibration number $\Omega = \omega_o \sqrt{\rho R_o^3 / \sigma}$ (as defined in Dorbolo *et al.* (2008)), we then compare their experimental reports to our simulation results for different values of the skidding friction parameter k. We use the comparison to define an adequate value of k for each Ω and complete our skidding friction model. We note, that since all other parameters involved in the definition of Ω are fixed for this study, Ω can be simply considered as a proxy for the droplet radius.

3.1.1 Optimal values of k

Protière *et al.* (2006) proposed a skidding friction model in which viscous effects yield a force that is proportional to droplet speed, where the proportionality constants were estimated on the basis of typical sizes for the contact area and air layer width. Moláček & Bush (2013*b*) presented a different skidding friction model in which the horizontal drag force due to the motion of the droplet as it slides on the surface is considered to be proportional to the vertical force exerted on the droplet, and to the droplet speed. They arrived at this form for the drag by means of experimental measurements of the horizontal coefficient of restitution of droplets impacting a bath at different angles. They go on to fit the resulting data of tangential coefficient of restitution as a function of the Weber number and interpret their findings as implying that the dominant effect for horizontal drag is momentum transference to the fluid bath. Moreover, they assume throughout their work that the pressed area is roughly constant.

Our present approach is similar to that of Protière *et al.* (2006); however, we are able to consider the change in contact area during each impact. We obtain, as shown in equation (52), a friction model that is proportional to the instantaneous value of the contact area and to the droplet's velocity. Nevertheless, in Galeano-Rios *et al.* (2017) it was shown that the pressed area and the vertical
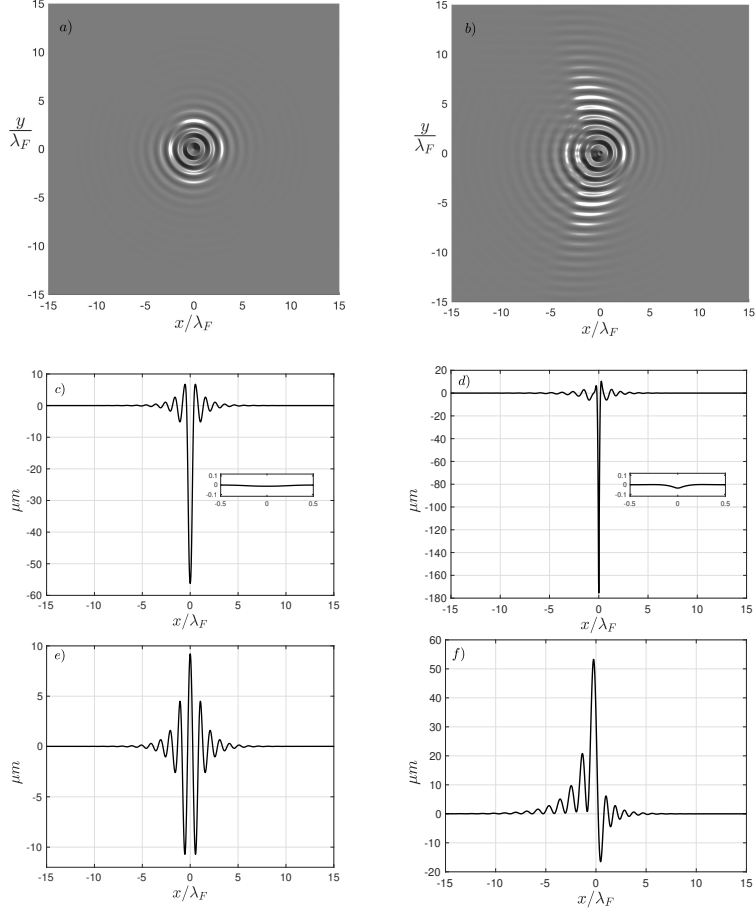
Figure 4: Wave field simulations for vibration number $\Omega = 0.8$, and drag parameter $k = 3100$. (a) Bouncer at $\Gamma/\Gamma_F = 0.74$, with (c) its cross-section at $y = 0$. (b) Walker moving to the right at $\Gamma/\Gamma_F = 0.98$ and (d) its section along the direction of walking. The wave field in a, b, c and d is sampled at the time of maximum absolute surface deflection and with $\boldsymbol{X}(t) = (0,0)$. The inset plots in panels c and d show a close up to the wave field at the impact location using the same vertical and horizontal scale (units of λ_F). The cross-sections in panels e and f are analogue to those in panels c and d, respectively; though in e and f the section is obtained just before a droplet impact. Animations of the wave field and droplet motion for these two simulations are included as supplementary material. We note that the figures do not show the totality of computational domain.

22
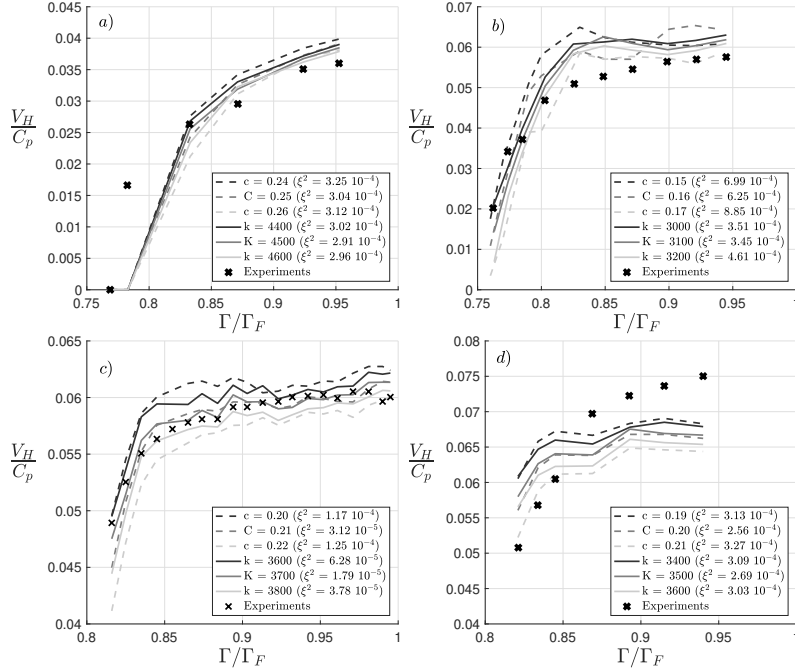
Figure 5: Walker speed as a function of Γ for different values of the drag parameter k, normalised by Faraday wave phase velocity ($C_p = 19\,\text{cm/s}$ in experiments, and $C_p = 19.88\,\text{cm/s}$ in simulations). (a) $\Omega = 0.7$, (b) $\Omega = 0.8$, (c) $\Omega = 0.83$, (d) $\Omega = 0.86$. Dashed lines correspond to the skidding friction model presented in Moláček & Bush (2013b), solid lines correspond to the skidding friction model developed in the present work. Experimental data for (a), (b) and (d), obtained from Moláček & Bush (2013b), data for (c) from Pucci *et al.* (2016)

force are roughly proportional, therefore, a model that accounts for pressed area variations will produce a skidding friction term that is approximately proportional to forces and droplet speeds. Thus, when we account for the effects of the varying pressed area, we can re-interpret the findings of Moláček & Bush (2013b) as not being incompatible with those of Protière *et al.* (2006). In particular, we can justify the form of the friction term given in Moláček & Bush (2013b) whilst still considering viscous effects as the main drivers of the resistance to motion during contact.

To find the optimal value K of the proportionality constant k for each droplet size (i.e. Ω) for which the walking speed was reported at different driving accelerations in the experimental works, we test a sequence of values of k. For each tested k we find the differences ξ_i between the experimental report for horizontal speed u_i^e and the average horizontal speed as calculated from the simulations u_i^s, where the i-th experimental point corresponds to a given value

of Γ_i/Γ_F (see figure 5). We thus define the total squared error for each attempted value of the drag parameter k as:

$$\xi^2(k,\Omega) = \sum_{i=1}^{n} \xi_i^2(k, \Omega, \Gamma_i/\Gamma_F) = \sum_{i=1}^{n} (u_i^e - u_i^s)^2 (k, \Omega, \Gamma_i/\Gamma_F), \qquad (78)$$

and we define

$$K(\Omega) = \operatorname{argmin} \xi^2(\cdot, \Omega). \qquad (79)$$

The values of $K(\Omega)$ are identified up to two significant figures and are reported in figure 5. Figure 6(a) shows the distribution of $K(\Omega)$. We perform an entirely analogous calculation, using the friction model presented in Moláček & Bush (2013b), in which $F_D = -c\sqrt{\rho R_o/\sigma} F(t)\mathbf{X}_t$, and we obtain a similar distribution of values for the corresponding optimal proportionality constant $C(\Omega)$. The respective walking speed predictions are reported in dashed lines in figure 5 and the distribution of $C(\Omega)$ is presented in figure 6(b). In practice, the value of C used in different models ranges from 0.1 to 0.35, as can be seen in the literature (Moláček & Bush, 2013b; Oza *et al.*, 2013; Milewski *et al.*, 2015; Durey & Milewski, 2017).

The agreement between theory and experiment shown in figure 5 is overall good, especially when considering the simplifications introduced; however, there clearly is room for improvement. The choice to stop at two significant figures in determining K is based on the fact that the two neighbouring values at that precision provide an obvious bound to how much the predictions can be improved by a more precise value of K, which indicate that no qualitative agreement is likely to be gained. A more complete understanding of the air flow in the intervening air layer would enable the production of better reduced models; as it would allow for a realistic treatment of the dependence of the $\bar{k}$ scaling factor on time or pressure distribution, and also of the time varying air layer width e. As part of our ongoing work, we have posed the problem including a coupled lubrication theory equation which we will attempt to address once we have successfully incorporated droplet deformations.

The skidding friction parameter k is $O(10^3)$ and $|A^a(t)|/(\pi R_0^2)$ (i.e. the fraction of the droplet's "shadow" that is pressed) is $O(10^{-1})$. Therefore the $k|A^a(t)|/(\pi R_0^2)$ is $O(10^2)$, which is significantly larger than 6 (the factor that corresponds to Stokes' drag). This verifies the intuition suggested at the end of section 2.4.1. Moreover, the value of $1/Ma$ (the reciprocal of the dimensionless mass of the droplet) ranges from 425 (biggest walking droplets) to 1334 (smallest walking droplets). This is consistent with walking droplet motion being dominated by the forces exerted by the waves onto the droplets, and also with bigger droplets, such as the superwalker considered in section 4.1 (for which $1/Ma = 93$), being less prone to walking under single frequency forcing.

The similarity between figures 6(a) and 6(b) is consistent with the finding of the approximate proportionality between vertical force and pressed area reported in Galeano-Rios *et al.* (2017). We notice that our proposed skidding friction model produces less total errors ($\xi^2(K(\Omega), \Omega)$) for most values of Ω
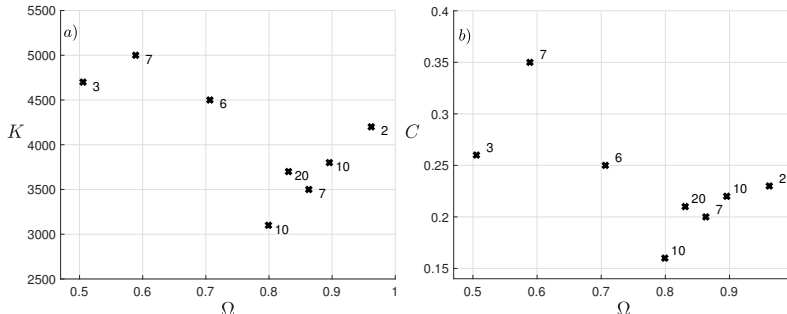
Figure 6: Skidding friction coefficients for the two models here considered. Panel (a) shows $K(\Omega)$ for the proposed model, panel (b) shows $C(\Omega)$ for the model in Moláček & Bush (2013*b*). Numbers along the markers indicate the number of data points available in the literature for a given droplet size.

and that the relative deviation with respect to the mean value is smaller for K ($\sigma_d(K_i)/\bar{K} = 0.16$, $\sigma_d(C_i)/\bar{C} = 0.24$). In what follows, we use $K(\Omega)$ for each droplet radius.

4   Comparisons to experiments of walking and bouncing droplets

Our model is completed with the specification of the skidding friction parameter. We thus proceed to simulating various experiments reported in the literature, across a range of physical parameters (Γ, Ω). In particular, we will compare the many walking and bouncing states observed and the details of the wave field and impact phases.

We vary Ω over the range of values typically used in experiments and with the driving amplitude Γ ranging from bouncing threshold to Faraday threshold. We compare the resulting steady state bouncers and walkers to the experimental results reported in Wind-Willassen *et al.* (2013). The results are summarised in figure 7, where squares (bouncers) and circles (walkers) indicate experimental reports and the background corresponds to our simulation results. The colour coding is shared between squares, circles and background. The red curve encloses the region in which the droplets walk in simulations and the vertical yellow dashed line indicates $\Gamma = 1$, to the right of which the driving acceleration reverses the sign of the gravity (in the frame of reference of the bath), during part of the cycle. The hashed region describes $(2,2)^2$ bouncers, which could easily be mistaken for $(2,1)$ bouncers, as was reported in Galeano-Rios *et al.* (2017) and observed experimentally by Couchman *et al.* (2018).

We note that, in figure 7, the comparison to experimental results is excellent, with the exception of cases for which even the experimental distinction of bouncing modes is challenging. In particular, the agreement with experimen-
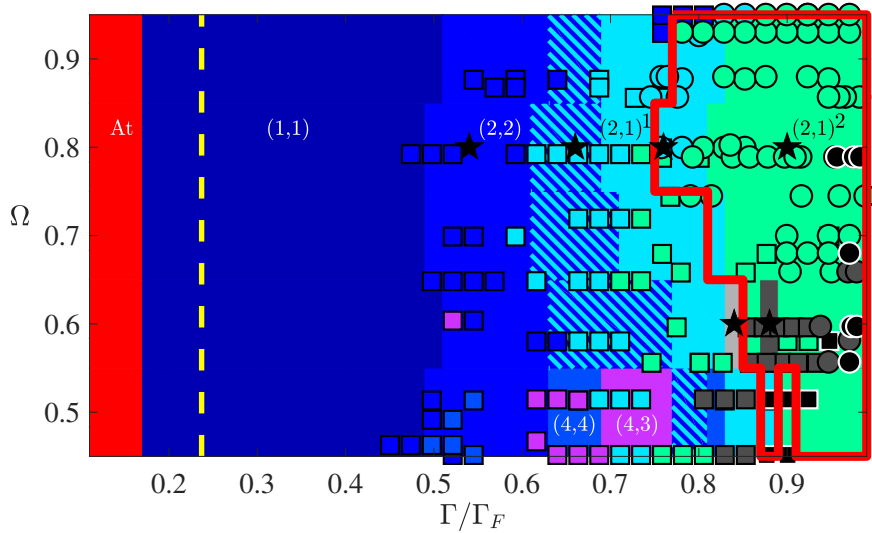
Figure 7: Phase diagram for bouncing and walking droplets. Bullets indicate experimental reports of the modes of bouncing (Wind-Willassen *et al.*, 2013), background colouring corresponds to the bouncing mode found in our simulations. The bouncing mode colour-coding is the same for bullets and background. The leftmost region (red) indicates the range of Γ for which our droplets are always in contact with the bath and the vertical yellow dashed line indicates $\Gamma = 1$. The red curve encloses the region in which the droplets walk in simulations. Grey regions correspond to $(4, 2)$ modes, light grey to $(4, 2)^1$ and dark grey to $(4, 2)^2$; chaotic bouncing is shown in black. The six ★ markers indicate the bouncing and walking modes shown in figure 8. The hashed region corresponds to $(2, 2)^2$ modes, which in Wind-Willassen *et al.* (2013) were classified as $(2, 1)$, but were later revealed by Damiano (2015*b*) to be less obvious instances of a $(2, 2)$ mode (see figure 8a and 8b for details).
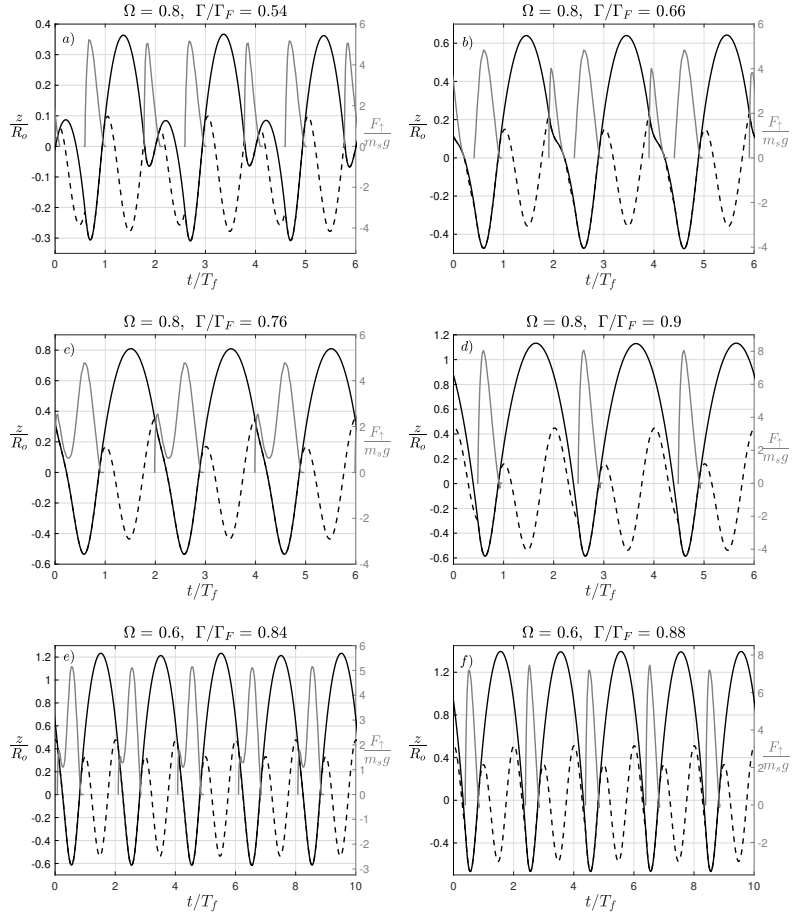
Figure 8: Variants of the same (m, n) mode. Solid black lines depict the height of the south pole of the droplet, dashed black lines indicate the point on the free surface that is directly below the south pole; all with respect to an inertial observer in the laboratory. Grey lines correspond to the vertical force on the droplet $F_\uparrow$. (a) $(2, 2)^1$ mode, in which the droplet reverses the direction of its vertical motion during both impacts. (b) $(2, 2)^2$ mode, in which the droplet reverses its vertical direction of motion every other impact. (c) $(2, 1)^1$ mode, in which the vertical force has two clearly marked maxima. (d) $(2, 1)^2$ mode, in which the vertical force shows a single peak. (e) $(4, 2)^1$ mode, which arises as a period doubling bifurcation from the $(2, 1)^1$ mode with all bounces producing vertical forces with two clear peaks but consecutive bounces have different force profiles. (f) $(4, 2)^2$ mode, which results from a period doubling bifurcation of the $(2, 1)^2$ mode.

27

tal results is substantially improved with respect to the most detailed walking droplet model that was previously available (see figure 4 in Milewski *et al.* (2015)). These improved walker prediction are obtained whilst also doing away with three parameters and solving realistic and detailed impact dynamics. Furthermore, this model is also able to capture all bouncing droplet phenomena reported in figure 10 of Galeano-Rios *et al.* (2017), with improved accuracy.

Figure 8 shows the three observed instances in which we distinguish two kinds of bouncing modes that are characterised by the same (m, n) notation. Panels (a) and (b) show two qualitatively different $(2, 2)$ modes. We refer to the mode in panel (a) as the $(2, 2)^1$ mode, in which the vertical motion of the droplet actually reverses direction four times over a period of motion, and as the $(2, 2)^2$ mode to the one in panel (b), in which reversals only take place twice over a motion period. Panels (c) and (d) reveal the qualitative differences between the $(2, 1)^1$ and $(2, 1)^2$ modes; the clearest distinction between the two being given by the fact that the in the $(2, 1)^1$ mode (panel c), there are two maxima in the vertical force over a relatively long ($\approx T_f$) contact, whereas in the $(2, 1)^2$ mode (panel d) a single maximum in vertical force is attained. Finally, we are also able to distinguish a $(4, 2)^1$ mode (panel e) and a $(4, 2)^2$ mode (panel f), which result from period doubling bifurcations of the $(2, 1)^1$ and $(2, 1)^2$ modes, respectively. Moreover, the comparison between panels (b) and (c) illustrates the reason why $(2, 2)^2$ bouncers can easily be mistaken for $(2, 1)^1$ bouncers. In fact, the hashed region in figure 7 mostly coincides with experimental reports of $(2, 1)^1$ modes. However, a more detailed report in Damiano (2015*b*) shows that for $\Omega = 0.8$, the bouncers in the hashed regions actually correspond to the gradual shrinking of the interval between the two bounces; as described below.

Figure 9 shows the dependence of impact and lift-off times for driving accelerations ranging from the bouncing threshold to Faraday threshold. Along every vertical traverse, we can see the transitions undergone over a bouncing period, at a given Γ/Γ_F. The left end of the graph shows how a weak driving acceleration leads to longer contacts; which for low enough Γ, end up merging and causing the droplet to stay attached to the surface. In reality coalescence would occur in the vicinity of the left end of the graph; however, since we do not model the thin air layer dynamics in this work, we are not able to predict it accurately. As we move to the right in the graph, we can see first the $(1, 1)$ mode (between $\Gamma/\Gamma_F \approx 0.23$ and $\Gamma/\Gamma_F \approx 0.42$ in the experiments, and between $\Gamma/\Gamma_F \approx 0.17$ and $\Gamma/\Gamma_F \approx 0.49$ in the simulations), for which both contacts are identical except for a shift in time of one forcing period. The period doubling mechanism from the $(1, 1)$ mode into the $(2, 2)$ mode is evidenced in the middle section of the figure, where we see that consecutive contacts start to differ from each other. As Γ is increased further, the two contacts grow closer, finally merging into one long contact with two peaks in force (see figure 8c) that are inherited from each one of the two distinct bounces in the $(2, 2)$ mode. Further to the right of the graph, the contact time shortens and the force peaks fuse into a shorter pulse (see figure 8d) that takes place roughly during the same interval of time for which contact took place in the $(1, 1)$ mode, but in a period doubled state. For insight on how driving acceleration influences walking velocity
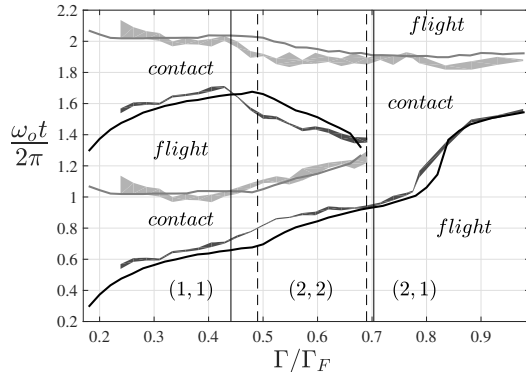
Figure 9: Evolution of the touch down and take off times as a function of the driving acceleration amplitude ($\Omega = 0.8$). The shaded regions indicate the experimental report in Damiano (2015b), of the start (dark) and end (light) of droplet contacts. The vertical width of each region corresponds to the experimental uncertainty in the measurements (Damiano, 2015a). The corresponding simulation results for impact and take off times are shown in black and grey lines, respectively. The vertical lines indicate the transition to a different (m, n) mode in experiment (solid) and simulations (dashed).

through changes in the vertical dynamics, figure (9) should be read alongside figure (5b).

A comparison between surface topography measurements (Damiano *et al.*, 2016) and our current wave field predicitons is shown in figure 10. In this figure we observe a similar agreement to that reported in figure 12 in Galeano-Rios *et al.* (2017), where the impact was computed directly onto the perturbed surface and not decomposed into an impact onto a flat surface and the unforced wave field evolution. This suggests that the separation of the problem into two has not affected our wave field predictions significantly. The disagreement observed is mostly in the magnitude of the wave elevation in the near field of the droplet. We believe the disparity here is mainly due to the shortcomings of the quasi-potential fluid formulation. It is important to highlight that, with the current fluid model, the wave length in experiments (≈ 4.75 mm, as reported by Pucci *et al.* (2016)) is slightly different from that predicted by our fluid model ($= 4.97$ mm).

4.1 Superwalkers: two frequency shaking

Valani *et al.* (2019) recently reported a new kind of walking droplets. These are relatively large droplets (up to 1.4 mm radius) that always bounce in place when the underlying bath is subject to simple harmonic motion, but walk particularly fast (up to about three times the maximum velocity for regular walkers, i.e. $C_w/C_p \approx 0.15$) when the bath is subject to vertical oscillations obtained
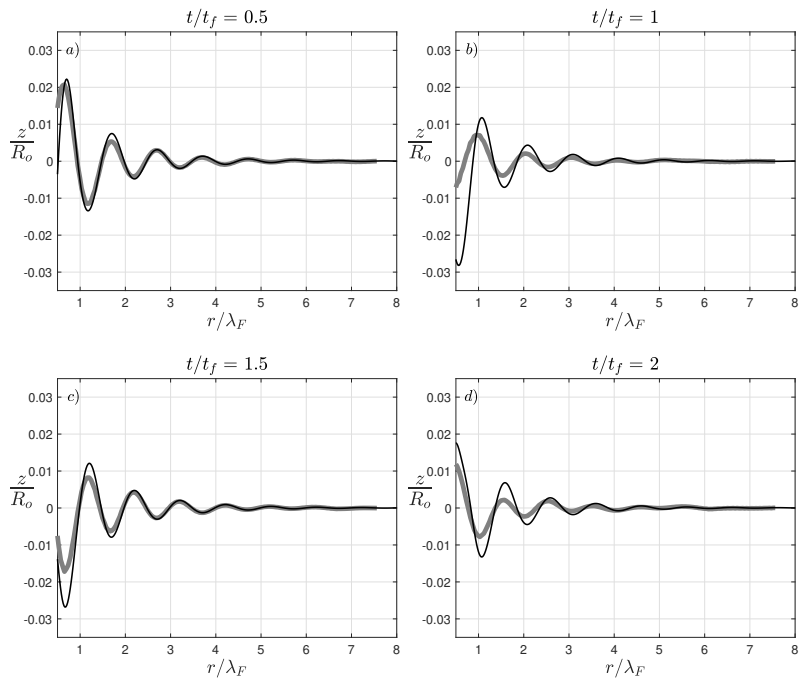
Figure 10: Comparison of wave field predictions to experimental measurements reported in Damiano *et al.* (2016). The wave field corresponds to a bouncer in the $(2,1)^1$ mode, $\Omega = 0.8$ and $\Gamma/\Gamma_F = 0.75$.

using the superposition of two sinusoidal signals of different frequencies. More specifically, this was observed to happen when the second frequency added is resonant with the subharmonic Faraday waves. The most relevant predecessor of this work is Sampara & Gilet (2016), who considered a combination of 80 Hz and 64 Hz forcing in a bath of 20 cSt silicone oil, and were thus able to find a series of novel trajectories for the walking droplet system.

Valani and collaborators drive the oil bath with a vertical acceleration of the form

$$z_{tt} = -g\left(\Gamma\cos\left(\omega_o t\right) + \Gamma^1\cos\left(\frac{\omega_o}{2}t + \theta_1\right)\right),\tag{80}$$

and therefore have two extra physical parameters with respect to the regular walking droplet experiment; namely the subharmonic forcing amplitude, controlled by Γ^1, and the phase shift between the two frequencies, given by θ_1. Regarding the bath motion, the two main differences between Sampara & Gilet (2016) and Valani *et al.* (2019) are the choice of the second frequency as resonant with the sub-harmonic Faraday waves and the introduction of the phase shift parameter, which was kept constant and equal to zero in Sampara & Gilet (2016). Moreover, the droplet size considered in Sampara & Gilet (2016) is in the regular walker size range. These differences explain why the superwalkers where not observed in their work.

The changes to the problem formulation, needed to model superwalkers, amount to replacing each instance of the expression

$$\frac{(1 - \Gamma\cos(4\pi t))}{Fr}\tag{81}$$

in equations (56), (57), (64), (65) and (71) by

$$\frac{(1 - \Gamma\cos(4\pi t) - \Gamma^1\cos(2\pi t + \theta_1))}{Fr},\tag{82}$$

and selecting an appropriate value for the skidding friction constant k. Another minor modification to simulate superwalkers is the use of a larger axisymmetric impact domain, i.e. a domain of radius $4\lambda_F$ (twice the diameter of the one used for regular walkers). This choice was made to guarantee that waves triggered by large droplets, which sometimes produce contacts that are twice as long as those of walkers, do not reach the boundary of the axisymmetric domain before the impact is over.

We highlight that superwalking droplets undergo a non-negligible amount of deformation. In particular, one can see that the droplet's Bond ($Bo_d = \rho g R^2/\sigma$) and Weber ($We_d = \rho R V_{\rm rel}^2/\sigma$) numbers are larger that those for regular walkers, which indicates that deformations induced by gravity and inertia will be more prevalent. Typical physical parameters for walking droplet yield $Bo_d = 0.0671$ and $We_d = 0.195$, whereas for the superwalkers considered here $Bo_d = 0.91$ and $We_d = 0.261$. Moreover, the ratio of walking speed C_w to the relative vertical speed before impact U_z is $C_w/U_z \approx 0.6$. We therefore consider that the main motivation for the present section is to demonstrate the surprising extent to
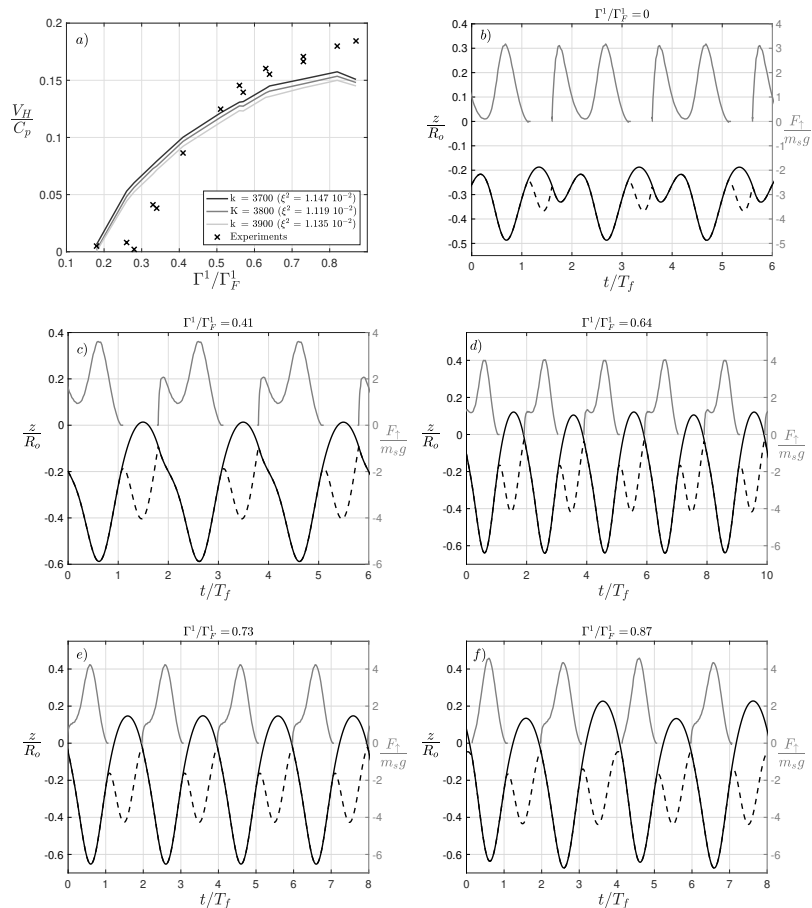
Figure 11: Superwalkers at $\Omega = 1.91$ ($R_o = 0.68\,\mathrm{mm}$), $\Gamma/\Gamma_F = 0.71$, $\theta_1 = 8\pi/9$. (a) Average velocity of superwalkers for different values of the drag parameter k, normalised by the phase velocity of the Faraday wave of frequency 40 Hz($C_p = 19\,\mathrm{cm/s}$ in experiments, and $C_p = 19.88\,\mathrm{cm/s}$ in the simulations). Vertical trajectories of the south pole (solid black lines) and of the free surface point just underneath (dashed lines), together with vertical forces $F_\uparrow$ on droplets for different driving accelerations Γ^1. Panels b to f show: a droplet bouncing at single frequency forcing in the $(2,1)^1$ mode (b), walking in the $(2,1)^1$ mode (c), walking in the $(4,2)^1$ mode (d), walking in the $(2,1)^2$ mode (e), and walking in the $(4,2)^2$ mode (f). Experimental data in panel a was obtained from Valani $et\ al.$ (2018).

32

which a model based on a non-deforming droplet can capture (super)walking droplet phenomena.

In figure 3(a) of Valani *et al.* (2019), it is shown that superwalkers only appear in a window of the θ_1 parameter that is centred roughly about $\theta_1 = 7\pi/9$. Moreover, in figure 2(c) of Valani *et al.* (2018), the walking speed of a superwalker of $R_o = 0.68$ mm for fixed $\Gamma/\Gamma_F = 0.71$ and $\theta_1 = 8\pi/9$, is reported as a function of Γ^1/Γ_F^1, with Γ_F^1 given by the Faraday threshold for the fluid bath when driven at an angular frequency of $\omega_o/2$. The superwalker phenomenon is reproduced for any value of the drag parameter k in the order of the values chosen for $K(\Omega)$ (figure 6). That is to say, droplets bounce when in the presence of a single frequency and walk faster than typical walkers (up to more than twice as fast as the fastest walkers) when the second frequency is added to the driving. To find the optimal $K(\Omega)$ for $\Omega(R_o = 0.68)$, we test different values of k and find the one that minimises the squared error with respect to the experimental results reported in figure 2(c) of Valani *et al.* (2018).

Figure 11(a) shows the comparison between experimental report of superwalker velocity (Valani *et al.*, 2019) and our simulation results for values of k in the vicinity of its optimal value $K(\Omega = 1.91)$. Figure 11(b-f) show the modes of bouncing displayed and the forces on the droplet due to collisions with the bath. When in the presence of a single frequency forcing (figure 11b), $\Gamma_1 = 0$; the droplet bounces in place displaying a $(2,1)^1$ mode with a particularly long contact. We note that our model shows in fact that the superwalkers are barely lifting off the surface when a single frequency is present. As the second frequency is introduced (panels c-f), the droplet walks even for Γ^1/Γ_F^1 as low as 0.18 (figure 11a and 11b). Like in the case of the walkers, the mode of bouncing observed changes with the driving acceleration (Γ^1, in this case). In figure 11, we see superwalkers bifurcation sequence: $(2,1)^1 \rightarrow (4,2)^1 \rightarrow (2,1)^2 \rightarrow (4,2)^2$. It is worth noting that, even though the skidding friction coefficient is of the same order as the one used for regular walkers, the walking speeds we obtain are in line with the superwalker experiments (up to three times the speed of single-frequency walkers).

We note that our model predicts that the superwalkers have a wave field that is qualitatively different to that of single-frequency walkers. As can be seen in figure 12(b), the wave field behind the superwalker does not exhibit, for these parameters, the typical interference pattern reported by Eddi *et al.* (2011), also observable in figure 4(b). Experimental reports from Valani *et al.* (2019) show that the wave field of the superwalkers indeed looks like our predictions. This distinctive wave field is likely due to the fact that we are exciting Faraday waves under two-frequency forcing, which will respond to a Mathieu equation that is different from the one for single frequency forcing found by Benjamin & Ursell (1954), see Zhang & Vinals (1997). In particular, the Fourier transform of the wave field contains a higher contribution of wavelengths in the range of the Faraday wavelength for 40 Hz forcing ($k \approx 7.16$ cm^{-1}). Moreover, the wave field associated to such a large droplet deforms the free surface substantially in the vicinity of the droplet, as can also be seen in figures 11(b-f), even in the absence of a second forcing frequency (figures 11b and 12a). We highlight that
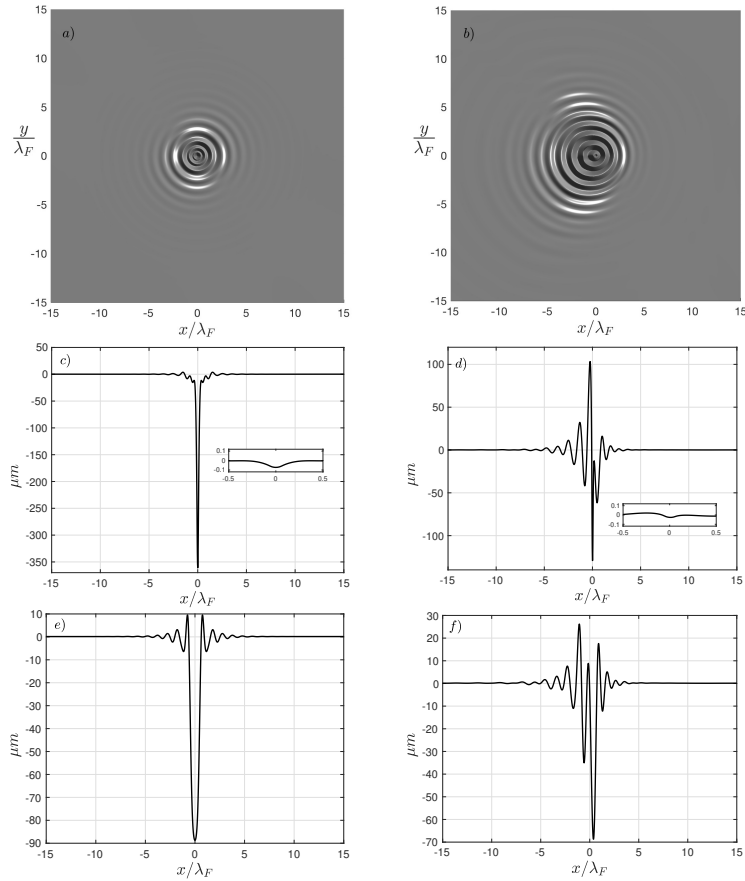
Figure 12: Wave field predictions for $\Omega = 1.91$, $\Gamma/\Gamma_F = 0.71$, $\theta_1 = 8\pi/9$. (a) Bouncer at $\Gamma^1/\Gamma_F^1 = 0$, and (b) superwalker moving to the right at $\Gamma^1/\Gamma_F^1 = 0.87$. Panels c and d show cross-sections of the wave field represented in a and b, respectively. The wave fields in a, b, c and d are sampled at the time at which the maximum surface deflection (in absolute value) occurs while the droplet is located at $\boldsymbol{X}(t) = (0,0)$. Inset plots in panels c and d show the impact location using the same scale for the vertical and horizontal axes (units of λ_F). Panels e and f show the respective analogue cross-section, to c and d; though taken just before a droplet impact. Animations of the wave field and droplet motion for these two simulations are included as supplementary material.

the inset plots in panels *c* and *d* show that the surface remains smooth at the impact location. This can also be appreciated in the corresponding animation of the simulations results from the cases in figure 12, which are provided as supplementary material.

To the best of our knowledge, no other model has captured superwalker phenomena. In particular, we attempted to use the model presented in Milewski *et al.* (2015) and obtained a significant mismatch in the vertical dynamics.

The superwalker phenomenon is one more piece of evidence of the extremely rich dynamics associated with the bouncing droplet system. A more complete treatment of superwalkers requires the consideration of droplet deformation and will be the subject of future work.

5   Discussion

We have described a general methodology to study impacts and rebounds at capillary scale. The method relies on the assumption that the impacting object does not become immersed and that we have a theory for the evolution of the capillary contact angle. When we apply the methodology to Faraday walkers, after a series of approximations, we arrive at a walker model that combines a quasi-potential fluid model with the superposition of translated axisymmetric impacts. We obtain a highly realistic walking droplet model that solves repeated bounces with minimal assumptions on the nature of the impact. The use of few assumptions enables the generation of a great amount of detailed predictions for the physical system. We carefully compare these predictions to experimental reports available in the literature obtaining an overall remarkable agreement.

We highlight the fact that our system is able to capture extremely well the majority of phenomena here tested. This is a strong indication that droplet deformation plays a relatively minor role in the overall dynamics of the walking droplet system; except possibly for superwalkers, for which our walking speed predictions deviate slightly more from the experimental reports. These deviations from our predictions are not unexpected, as droplet deformation is known to be non-negligible in this case. An adaptation of the kinematic match method which couples the deformation of the impacting droplet to the fluid equations is underway, its implementation should result in a substantial improvement for our superwalker predictions and it should provide the tools to assess precisely the extent to which the results change when the impacting object is compliant. To account for inertial effects in droplet deformation during impact, we need to approximate the fluid flow inside the droplet. Moreover, the decomposition of the impact into vertical and horizontal motion, though in principle still possible, requires the observation of some additional effects (Purvis & Smith, 2005).

Single bounce dynamics, similar to those observed in bouncing droplets, have been obtained for solid spheres (see for instance Lee & Kim (2008) and Bauman *et al.* (2019)); however, sustained *periodic* bouncing and walking regimes have not been reproduced with solids. Surface roughness of solids at the scale of the air layer width, which can puncture the lubrication layer, could be the cause.

It is also possible that deformation plays a role in preserving the integrity of the air layer; nevertheless, our present work strongly suggests that the role of these deformations is otherwise relatively minor in terms of the overall dynamic behaviour for the parameter regime here considered (see for instance figure 9). Moreover, droplet deformations have been shown to play an important role when the fluid of the bath is significantly less compliant than that of the droplet (see Terwagne *et al.* (2013)). Such a system can also be studied using a kinematic match method for deformable impactors. Deformation in bouncing, walking and superwalking droplets will be the subject of a separate study, which will also consider more general two-frequency forcing bouncing droplet systems, including the system reported by Sampara & Gilet (2016). This future work will allow us to quantify dynamic droplet deformation and can be compared to experimental measurements of droplet deformation reported by Couchman *et al.* (2018), indicating at most a 5% radial deformation for single frequency walkers. Similarly, in a private communication with the lead author of Valani *et al.* (2019) it was reported that superwalkers of the size here considered show a radial deformation of at most 9%.

Our work re-enforces the well established notion that translating axisymmetric impacts provides a sufficiently good approximation when modelling walkers. This is also in agreement with the more general notion that the horizontal component of impact velocity has a negligible role in solid-impact problems unless it is significantly large (see for instance Moore *et al.* (2012)), which is one of Trefethen's paradoxes (Trefethen & Panton, 1990). Moreover, we make use of the linear nature of the waves in this problem to decompose its solution into two parts, which introduces the possibility of using different methods to solve the impact and the wave evolution. One can then use the optimal method for each part and arrive more efficiently at a more accurate solution to the full problem, once they are combined. Consequently, in this work, we solve bouncers and walkers in less than half the computation time as required for the bouncer only simulations in Galeano-Rios *et al.* (2017) and at four time increased spatial accuracy. Another important consequence of successfully separating the problem into two is that this allows for the possibility of solving the unforced waves with other, perhaps more elaborate, fluid models which might be solved very efficiently when unforced by surface pressures but with which it would prove challenging to solve numerous impacts.

Many walking droplet experiments involve complex interactions between the impact phase and the droplet trajectory. This is expected to be the case in confined chaotic motion in a potential (Perrard *et al.*, 2014; Durey *et al.*, 2018) or in a corral (Harris *et al.*, 2013). For long time realistic computations of such problems, where the impacts may vary chaotically, we could accelerate simulations by pre-computing a library of droplet impacts with the surface, i.e. a database of axisymmetric solutions parameterised by relative impact velocity and impact phase, from which the resultant wave field and droplet forces can be recalled, the droplet trajectory calculated, and the new wave field superposed onto the preexisting wave field. This approach is currently being developed to realistically introduce the effect of impact phase variations in 2D models of

tunnelling and two particle correlations, such as those in Nachbin *et al.* (2017) and Nachbin (2018).

Detailed wave field predictions have proven to be fundamental to capture droplet-droplet interactions, as the role of moving wave fronts and subtle changes in impact phases define the direction of the horizontal forces on the droplets bouncing in close range (Galeano-Rios *et al.*, 2018). The next order approximation for the fluid motion in the bath is given by the linearised Navier-Stokes equations for incompressible flow (Galeano-Rios, 2016; Durey, 2018; Tadrist *et al.*, 2018), which are non-local in time (Prosperetti, 1976; Beyer & Friedrich, 1995). In view of our present results, it seems clear that a combination of the solution of the linearised Navier-Stokes equations with a library of impacts is likely the most adequate approach to study multi-droplet systems in great detail.

Multi-droplet systems are the subject of particular interest, as they are a realisation of an active matter system in which the "agents" take energy from the waves and also interact through them. Moreover, other collections of surface bounded objects would provide similar examples of wave-mediated active matter systems which can be modelled with relatively simple modifications of the methods here presented.

A   Physical constants

Air:
$$\mu_{\mathrm{air}} = 1.8 \times 10^{-4}\,\mathrm{gr\,cm^{-1}\,s^{-1}}. \tag{83}$$

Silicone Oil:
$$\sigma = 20.6\ \mathrm{dyne\,cm^{-1}}, \tag{84}$$

$$\rho = 0.949\ \mathrm{gr\,cm^{-3}}, \tag{85}$$

$$\nu = \mu/\rho = 0.2\ \mathrm{St} = 0.2\ \mathrm{cm^2\,s^{-1}}. \tag{86}$$

Gravity in the frame of reference of the bath:
$$g = 980\,\mathrm{cm\,s^{-2}}, \tag{87}$$

$$\Gamma_F = 4.22\,g = 4135\,\mathrm{cm\,s^{-2}}, \tag{88}$$

$$\Gamma_F^1 = 1.19\,g = 1166\,\mathrm{cm\,s^{-2}}, \tag{89}$$

$$\omega_o = 2\pi\,80\,\mathrm{rad\,s^{-1}}, \tag{90}$$

References

Bauman, I., MacEwen, A. & Harris, D. M. 2019 Rebound dynamics of superhydrophobic spheres. *In preparation* − (−), −.

Benjamin, T. B. & Ursell, F. 1954 The stability of the plane free surface of a liquid in vertical periodic motion. *Proc. R. Soc. Lond. A* **225**, 505–515.

Beyer, J & Friedrich, R 1995 Faraday instability: linear analysis for viscous fluids. *Physical Review E* **51** (2), 1162.

Bush, J. W. M. 2015 Pilot-wave hydrodynamics. *Annu. Rev. Fluid Mech.* **47**, 269–292.

Bush, J. W. M., Couder, Y., Gilet, T., Milewski, P. A. & Nachbin, A. 2018 Introduction to focus issue on hydrodynamic quantum analogs. *Chaos: An Interdisciplinary Journal of Nonlinear Science* **28** (9), 096001.

Bush, J. W. M. & Hu, D. L. 2006 Walking on water: biolocomotion at the interface. *Annu. Rev. Fluid Mech.* **38**, 339–369.

Couchman, M. M. P., Turton, S. E. & Bush, J. W. M. 2018 Experimental resolution and theoretical modelling of bouncing phase variations in pilot-wave hydrodynamics. *J. Fluid Mech.* **Submitted**, −.

Couder, Y., Fort, E., Gautier, C. H. & Boudaoud, A. 2005*a* From bouncing to floating: Noncoalescence of drops on a fluid bath. *Phys. Rev. Lett.* **94** (177801).

Couder, Y., Protière, S., Fort, E. & Boudaoud, A. 2005*b* Walking and orbiting droplets. *Nature* **437** (208).

Damiano, A. P. 2015*a* personal communication.

Damiano, A. P. 2015*b* Surface topography measurements of the bouncing droplet experiment. Master's thesis, École Polytechnique Fédérale de Lausanne.

Damiano, A. P., Brun, P.-T., Harris, D. M., Galeano-Rios, C. A. & Bush, J. W. M. 2016 Surface topography measurements of the bouncing droplet experiment. *Experiments in Fluids* **57** (10), 163.

Dorbolo, S., Terwagne, D., Vandewalle, N. & Gilet, T. 2008 Resonant and rolling droplet. *New Journal of Physics* **10** (11), 113021.

Durey, M. 2018 Faraday wave-droplet dynamics: a hydrodynamic quantum analogue. PhD thesis, University of Bath.

Durey, M. & Milewski, P. A. 2017 Faraday wave–droplet dynamics: discrete-time analysis. *J. Fluid Mech.* **821**, 296–329.

Durey, M., Milewski, P. A. & Bush, J. W. M. 2018 Dynamics, emergent statistics, and the mean-pilot-wave potential of walking droplets. *Chaos: An Interdisciplinary Journal of Nonlinear Science* **28** (9), 096108.

Eddi, A., Sultan, R., Moukhtar, J., Fort, E., Rossi, M. & Couder, Y. 2011 Information stored in faraday waves: the origin of a path memory. *J. Fluid Mech.* **674**, 433–463.

Galeano-Rios, C. A. 2016 Hydrodynamic pilot-waves: Analytical modeling approaches to the interaction of drops and surface waves. PhD thesis, Instituto Nacional de Matemática Pura e Aplicada.

Galeano-Rios, C. A., Couchman, M. M. P., Caldairou, P. & Bush, J. W. M. 2018 Ratcheting droplet pairs. *Chaos: An Interdisciplinary Journal of Nonlinear Science* **28** (9), 096112.

Galeano-Rios, C. A., Milewski, P. A. & Vanden-Broeck, J.-M. 2017 Non-wetting impact of a sphere onto a bath and its application to bouncing droplets. *J. Fluid Mech.* **826**, 97–127.

Gilet, T. & Bush, J. W. M. 2009 The fluid trampoline: droplets bouncing on a soap film. *J. Fluid Mech.* **625**, 167–203.

Harris, D. M., Moukhtar, J., Fort, E., Couder, Y. & Bush, J. W. M. 2013 Wavelike statistics from pilot-wave dynamics in a circular corral. *Phys. Rev. E* **88** (011001).

Ho, D. T., Bliven, L. F., Wanninkhof, R. I. K. & Schlosser, P. 1997 The effect of rain on air-water gas exchange. *Tellus B* **49** (2), 149–158.

Howison, S. D., Ockendon, J. R. & Wilson, S. K. 1991 Incompressible water-entry problems at small deadrise angles. *J. Fluid Mech.* **222**, 215–230.

Korobkin, A. A. & Pukhnachov, V. V. 1988 Initial stage of water impact. *Ann. Rev. Fluid Mech.* **20** (1), 159–185.

Lee, D.-G. & Kim, H.-Y. 2008 Impact of a superhydrophobic sphere onto water. *Langmuir* **24**, 142–145.

Milewski, P., Galeano-Rios, C. A., Nachbin, A. & Bush, J. W. M. 2015 Faraday pilot-wave dynamics: modeling and computation. *J. Fluid Mech.* **778**, 361–388.

Moláček, J. & Bush, J. W. M. 2013a Drops bouncing on a vibrating bath. *J. Fluid Mech.* **727**, 582–611.

Moláček, J. & Bush, J. W. M. 2013b Drops walking on a vibrating bath: towards a hydrodynamic pilot-wave theory. *J. Fluid Mech.* **727**, 612–647.

MOORE, M. R., HOWISON, S. D., OCKENDON, J. R. & OLIVER, J. M. 2012 Three-dimensional oblique water-entry problems at small deadrise angles. *J. Fluid Mech.* **711**, 259–280.

NACHBIN, A. 2018 Walking droplets correlated at a distance. *Chaos: An Interdisciplinary Journal of Nonlinear Science* **28** (9), 096110.

NACHBIN, A., MILEWSKI, P. A. & BUSH, J. W. M. 2017 Tunneling with a hydrodynamic pilot-wave model. *Physical Review Fluids* **2** (3), 034801.

OZA, A. U., ROSALES, R. R. & BUSH, J. W. M. 2013 A trajectory equation for walking droplets: hydrodynamic pilot-wave theory. *J. Fluid Mech.* **737**, 552–570.

PERRARD, S., LABOUSSE, M., MISKIN, M., FORT, E. & COUDER, Y. 2014 Self-organization into quantized eigenstates of a classical wave-driven particle. *Nat. Commun.* **5** (3219).

PROSPERETTI, ANDREA 1976 Viscous effects on small-amplitude surface waves. *The Physics of Fluids* **19** (2), 195–203.

PROTIÈRE, S., BOUDAOUD, A. & COUDER, Y. 2006 Particle-wave association on a fluid interface. *J. Fluid Mech.* **554**, 85–108.

PUCCI, G., SÁENZ, P. J., FARIA, L. M. & BUSH, J. W. M. 2016 Non-specular reflection of walking droplets. *J. Fluid Mech.* **804**.

PURVIS, R. & SMITH, F. T. 2005 Droplet impact on water layers: post-impact analysis and computations. *Philosophical Transactions of the Royal Society A: Mathematical, Physical and Engineering Sciences* **363** (1830), 1209–1221.

SAMPARA, N. & GILET, T. 2016 Two-frequency forcing of droplet rebounds on a liquid bath. *Physical Review E* **94** (5), 053112.

TADRIST, LOÏC, SHIM, JEONG-BO, GILET, TRISTAN & SCHLAGHECK, PETER 2018 Faraday instability and subthreshold faraday waves: surface waves emitted by walkers. *Journal of Fluid Mechanics* **848**, 906–945.

TERWAGNE, D., LUDEWIG, F., VANDEWALLE, N. & DORBOLO, S. 2013 The role of droplet deformations in the bouncing droplet dynamics. *Physics of Fluids* **25** (122101).

TERWAGNE, D., VANDEWALLE, N. & DORBOLO, S. 2007 Lifetime of a bouncing droplet. *Phys. Rev. E* **76** (056311).

TREFETHEN, L. M. & PANTON, R. L. 1990 Some unanswered questions in fluid mechanics. *Applied Mechanics Reviews; (United States)* **43** (8).

VALANI, R. N., SLIM, A. C. & SIMULA, T. 2018 Superwalkers. *arXiv preprint* **arXiv:1807.06879**.

Valani, R. N., Slim, A. C. & Simula, T. 2019 Superwalking droplets. *Phys. Rev. Lett.* **Submitted**.

Wagner, H. 1932 Über stoß-und gleitvorgänge an der oberfläche von flüssigkeiten. *ZAMM-Journal of Applied Mathematics and Mechanics/Zeitschrift für Angewandte Mathematik und Mechanik* **12** (4), 193–215.

Wind-Willassen, O., Moláček, J., Harris, D. M. & Bush, J. W. M. 2013 Exotic states of bouncing and walking droplets. *Phys. Fluids* **25** (0820023).

Zhang, W. & Vinals, J. 1997 Pattern formation in weakly damped parametric surface waves driven by two frequency components. *J. Fluid Mech.* **341**, 225–244.

Zhbankova, S. L. & Kolpakov, A. V. 1990 Collision of water drops with a plane water surface. *Fluid Dynamics* **25** (3), 470–473.